TUBE WAVES IN ULTRA-DEEP WATERS: PRELIMINARY RESULTS

A Thesis

by

SATYAN SINGH

Submitted to the Office of Graduate Studies of
Texas A&M University
in partial fulfillment of the requirements for the degree of

MASTER OF SCIENCE

December 2011

Major Subject: Geophysics

Tube Waves in Ultra-deep Waters: Preliminary Results

TUBE WAVES IN ULTRA-DEEP WATERS: PRELIMINARY RESULTS

A Thesis

by

SATYAN SINGH

Submitted to the Office of Graduate Studies of
Texas A&M University
in partial fulfillment of the requirements for the degree of

MASTER OF SCIENCE

Approved by:

Chair of Committee,	Luc Ikelle
Committee Members,	Yuefeng Sun
	David Schechter
Head of Department,	Andreas Kronenberg

December 2011

Major Subject: Geophysics

ABSTRACT

Tube Waves in Ultra-deep Waters: Preliminary Results.

(December 2011)

Satyan Singh, B.S., University of the West Indies, St. Augustine

Chair of Advisory Committee: Dr. Luc Ikelle

The oil and gas industry defines ultra-deep-water regions as areas in which water depths are greater than 1500 m. It is now well established that there are hydrocarbons in these regions. The reservoirs in these areas are generally located below basalt rocks or below salts. The focus of this thesis is to understand reflections, refractions, diffractions and scattering for acoustic lenses located below basalt rocks. The results of this study can potentially be used to understand the effect of tube waves on borehole seismic data in ultra-deep waters.

Finite-difference modeling technique was used for this study. Finite-difference modeling allowed us to model refractions, reflections, diffractions and scattering; actually all events in surface seismic data, as well as borehole seismic data can be modeled. However, because of limited computational resources, this study will be based on a 2D finite difference instead of a 3D finite difference. This limitation implies that laterally infinite lenses were used to describe cylindrical boreholes.

The four main characteristics of the geological constructs used here in simulating the ultra-deep-water regions were the size of the water column, the topography of the sea floor, the interfaces of basalt layers with the surroundings rocks, and the structure of heterogeneities inside the basalt layers.

The average wavelength of wave propagation below the basalt layer is 125 m, which is very large compared to the size of a typical borehole (0.1 m). A lens with a thickness of 2.5 m, which corresponds to a dimension 50 times smaller than

the average wavelength, sub-basalt was constructed. Also included were some lateral extensions in the construction of the lens to simulate wash-out zones.

This study investigates the wave propagation below the basalt rocks and the effect of tube waves on borehole seismic data below the basalt layer by using these lenses instead of a cylindrical borehole. As the borehole geometry is different from that of the lens, the results are considered preliminary. Results suggest that tube waves are negligible in ultra-deep waters below basalt rocks because the wavelength of the seismic waves is large in comparison to the wash-out zone (192 times larger).

DEDICATION

To Darsel Seepersad, who has always been there to support and motivate me through my academic career, without her I would not have reached this far.

ACKNOWLEDGEMENTS

I would like to thank my committee chair, Dr. Ikelle, and my committee members, Dr. Sun, and Dr. Schechter, for their support throughout the course of this research. Also, thanks go to Dr. Everett for substituting for Dr. Sun.

Dr. Ikelle's advice and teachings have been very beneficial to my development, for which I will be eternally grateful. He has often gone above and beyond his capacity as a lecturer to lead me in the right direction. His student, Ibrahim Alukhail, has also helped me a great deal throughout my research.

Thanks also go to my friends and colleagues, as well as the department faculty and staff for making my time at Texas A&M University a great experience.

Finally, thanks to my mother and father for their encouragement and support through my entire academic career.

TABLE OF CONTENTS

Page

Page

LIST OF FIGURES

Page

Page

Page

Page

CHAPTER I

INTRODUCTION: BRIEF REVIEW OF TUBE WAVE-LIKE EVENTS

Our objective in this thesis is to investigate tube wave-like events in ultra-deep- water regions. We start by recalling tube wave-like events in the simplified standard geology of a homogeneous half-space with a horizontal lens in the middle, as shown in Figure 1.1. The lens is filled with water. The source is explosive and is discharged in the formation, which is 20 m away from the lens.

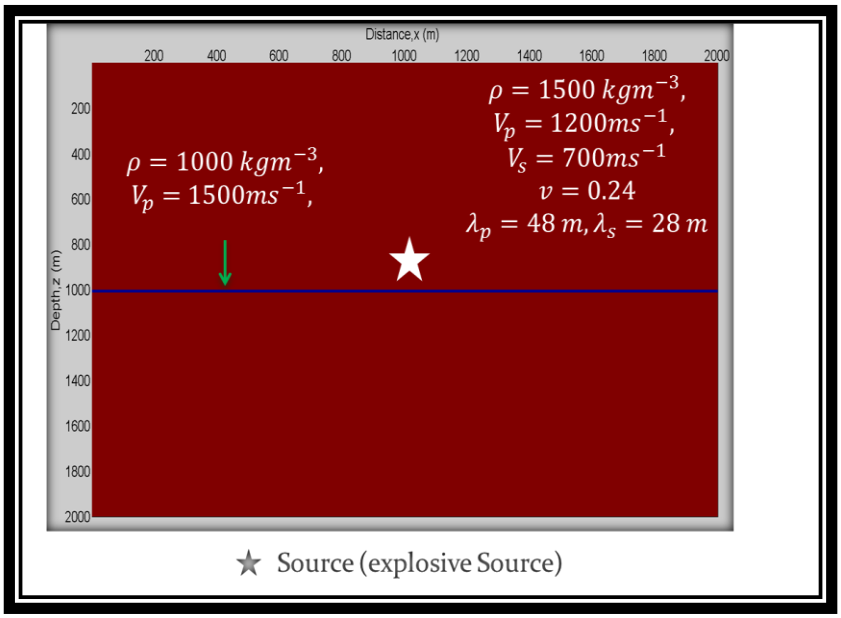

Figure 1.1. Homogeneous half-space separated by a lens where; ρ is density, V_p is velocity of the compressional wave, V_s is the velocity of the shear wave, v is the poisson ratio of the material, λ_p is the wavelength of the compressional wave and λ_s is the wavelength of the shear wave.

This thesis follows the style of Geophysics.

The corresponding borehole-like seismic data are shown in Figure 1.2. The finite difference modeling parameters are; time sampling of 4 ms, recording duration of 1.2 seconds, a grid size of 2 m, and 800 receivers at a spacing of 2 m. The receivers are placed in the lens, and the pressure is recorded.

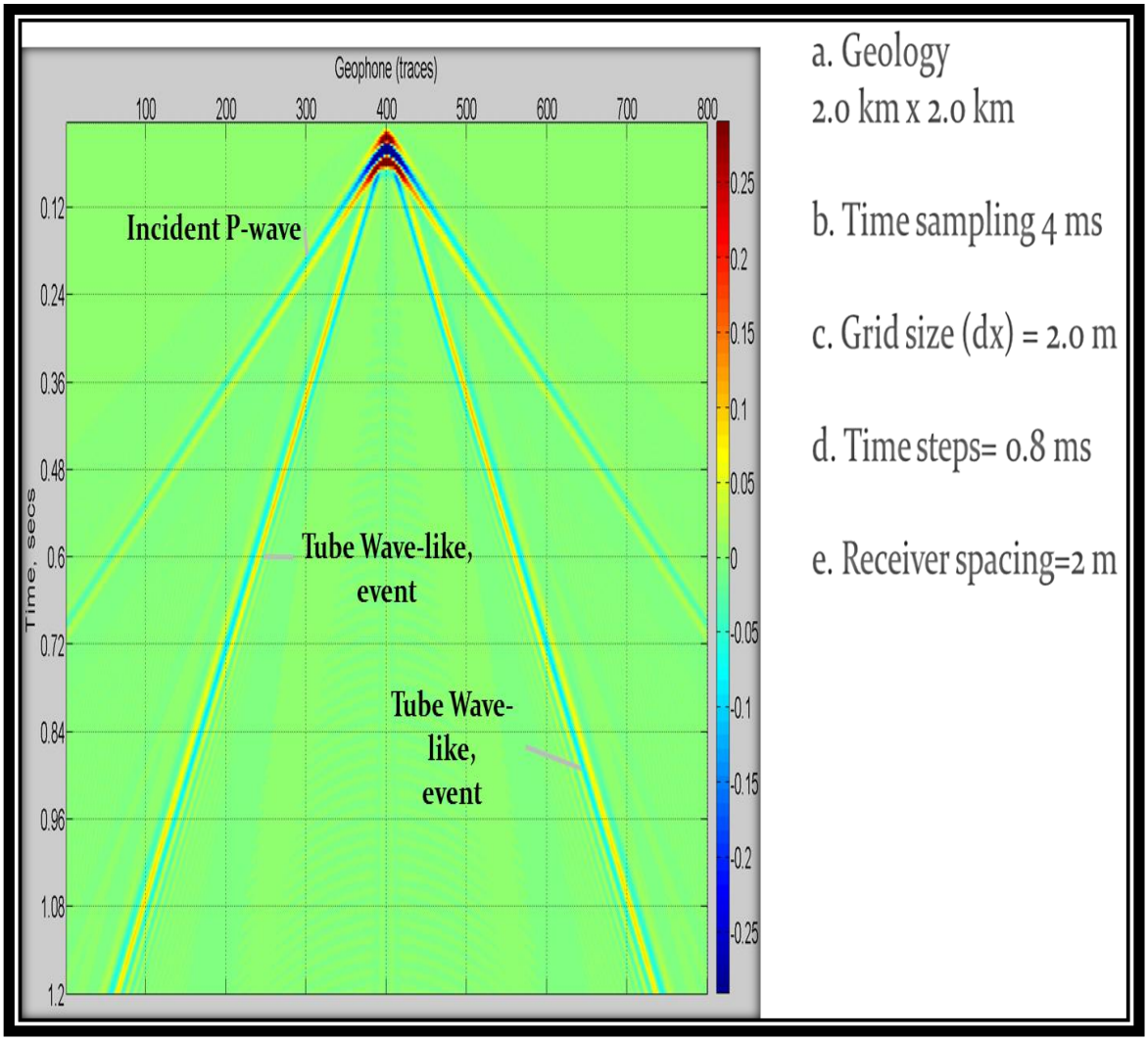

Figure 1.2. Borehole seismic data for geological construct 1.1, displaying tube wave-like events, and the physical quantity that is recorded is pressure.

The borehole-like seismic data have two events, as shown in Figure 1.2. The first event to be recorded is the direct primary wave. The second event to be recorded is the tube wave-like event. The measured velocity of the tube wave-like event from the borehole-like seismic data is 550 ms^{-1}. In the geological model there are no waves that propagate at this velocity. This event, which is smaller than all the velocities in the geologic model, including the lens fluid (1500 ms^{-1}), is characteristic of tube waves.

The tube waves are generally confined to propagating along the borehole. In other words, very little energy is released to the formation, as illustrated in Figure 1.3. This would imply that tube waves have high amplitudes; therefore they are considered a major source of noise in borehole seismic data (Ikelle and Amundsen, 2005). We can clearly see the high amplitude of the tube wave in comparison to the direct primary-wave event in Figure 1.2.

The snapshot is used to better understand the propagation of the tube waves, as shown in Figure 1.3. The snapshot is modeled by putting a receiver at every grid point in the model. Although not feasible in reality, it is a useful tool for visualization purposes. The snapshot is taken at 640 ms after the source has been fired. Each receiver in the snapshot records both pressure and horizontal particle velocity. The pressure data show the primary wave reflecting from the lens and the tube wave propagating in the lens. The horizontal particle velocity shows both the primary and shear waves reflected from the lens and the tube wave. The tube wave is identified by the “ringing” event. The snapshot also illustrates the characteristic slow velocity of the tube wave compared to the shear wave.

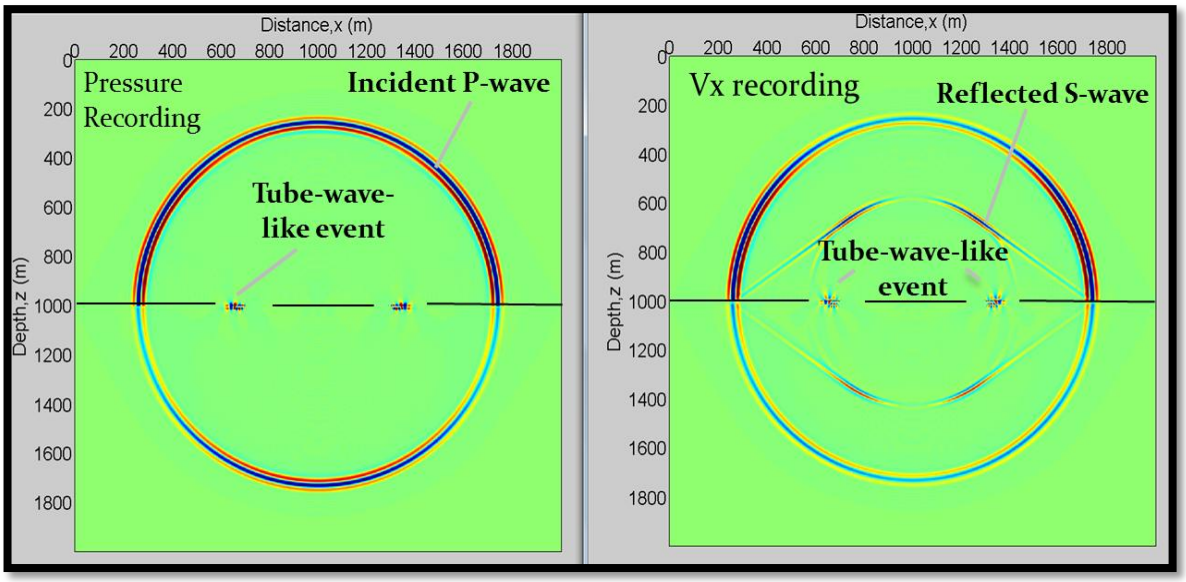

Figure 1.3. Wave propagation snapshot at 640 ms for geological construct in Figure 1.1, the physical quantity being measured is the pressure on the left and the horizontal particle velocity on the left.

Now that we have identified tube waves in standard geology, our objective is to investigate tube waves in ultra-deep waters.

CHAPTER II

A REVIEW OF WAVE PROPAGATION IN A TWO-HALF-SPACE MODEL SEPARATED BY A LENS

Introduction

The geology of ultra-deep-water regions, which include basalt layers, is generally very complex. This complexity will be discussed in Chapters II and III. In this chapter we consider a simplified model of ultra-deep-water regions with homogeneous flat basalt. We will take advantage of these simplifications to illustrate how borehole seismic data, with the borehole located below the basalt, are affected by the wavelength of the incoming wave, the shape and size of the borehole, and the wash-out of the borehole.

More precisely, our geological model here consists of two half-spaces. The top half-space corresponds to the basalt layer, and the bottom half-space corresponds to the sub-basalt layers. The second half-space is made of two layers, as illustrated in Figure 2.1. Through our study in this chapter, we assume that the physical properties of the basalt layer are fixed; only the elastic parameters of the bottom half-space vary. This variation allows us to evaluate different wavelengths.

Various scenarios of borehole geometries, including the horizontal borehole, will be considered. Wash-out zones will also be included in the borehole geometries.

Effect of Lens Size on Borehole-like Seismic Data

In this section we consider horizontal lenses, as illustrated in Figure 2.1. We filled it with water. The source is positioned in the basalt layer with a central frequency of 25 Hz, which corresponds to a wavelength of 192 m in the basalt layer. The receivers located inside the lens measure pressure.

We have computed seismic data using finite-difference modeling, (See Appendix A for a description of finite-difference modeling), for a 10 m, 5 m, and 2.5 m lens thickness. These thicknesses are more than 20 times smaller than the wavelength through the basalt. Let us start by looking at the results for the borehole with 10 m thickness, as shown in Figure 2.2. The modeling parameters for the borehole seismic data are; time sampling of 2.4 ms, a grid size of 2 m, and 850 receivers placed in the lens with a spacing of 2 m.

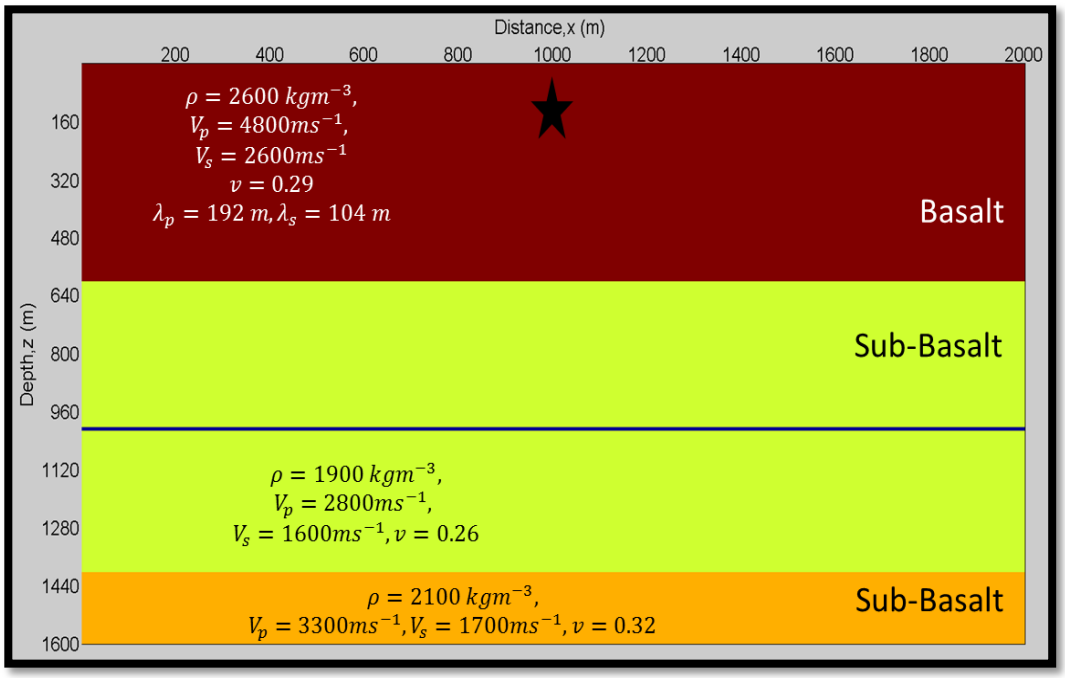

Figure 2.1. Geological construct of a lens (blue) of thickness 10 m inserted horizontally in the sub-basalt layer, the source is represented by ★, the hydrophones are placed along the middle of the lens.

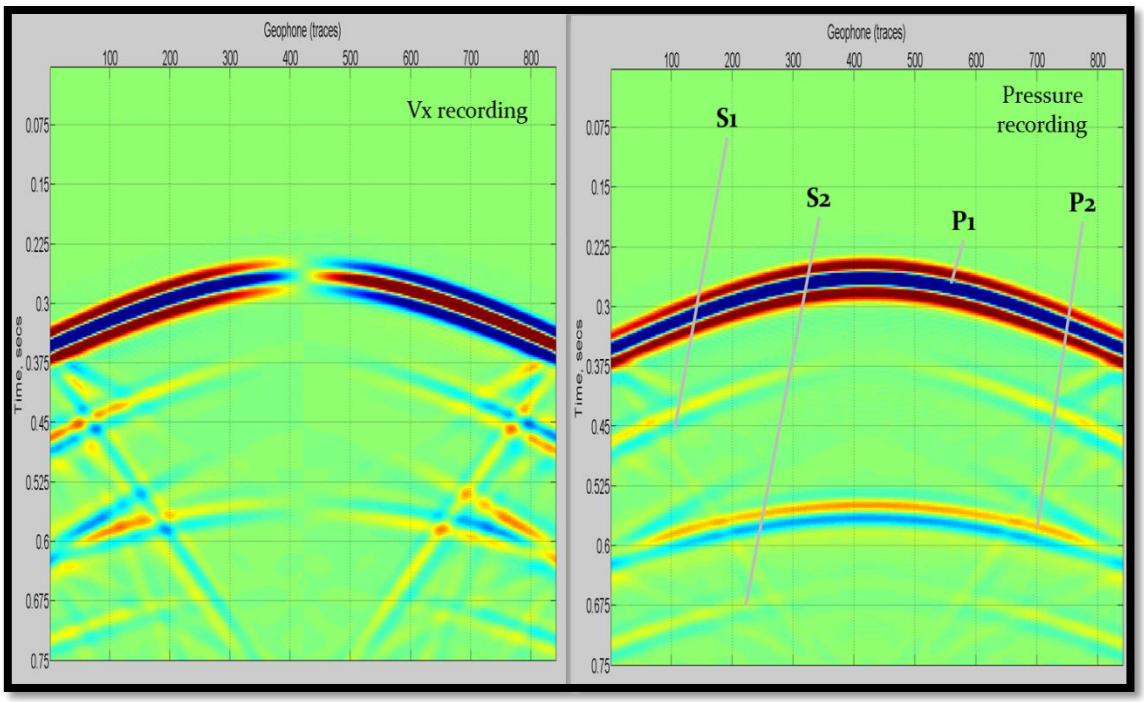

Figure 2.2. Borehole seismic data of geological construct in Figure 2.1, there are 850 hydrophones spaced at 2 m in the lens.

We will now describe the events shown in Figure 2.2. The first event that was recorded is the primary-wave event (P_1) when the direct primary wave is transmitted of the from the basalt half-space to the sub-basalt layer. S_1 is the event that is recorded due to the conversion of the direct primary wave to a shear wave when the direct primary wave has been transmitted into the sub-basalt layer. The P_2 event is the recording of a primary wave due to the reflection of the P_1 event from the top of the bottom half-space to the receivers. The last reflection in the P_2 case can also cause a propagating shear wave to be recorded at the receivers (S_2).

We are working in a 2D scenario. Therefore the lens acts as a plane and can reflect and refract seismic waves. The lens is located in the middle of the sub-basalt layer; hence the P_2 event is also caused by the reflection of the P_1 event from the lens, and then reflected from the base of the basalt layer to be recorded, as shown

in Figure 2.3 as the P_L event. Similarly, the S_2 events can be caused by the reflection of the P_1 event from the lens, and then reflected (P_1) from the base of the basalt layer to be recorded, as shown in Figure 2.3 as the S_L event.

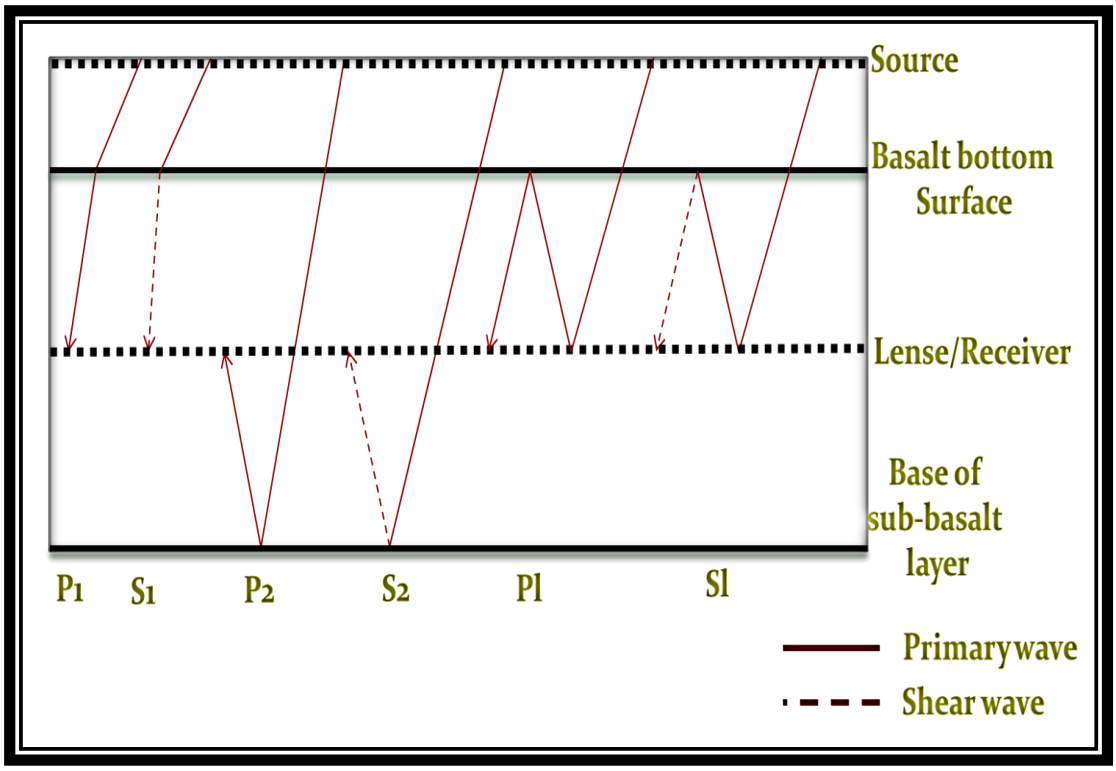

Figure 2.3. Schematic of some of the events that occur for an explosive source in the basalt layer in geological construct Figure 2.1.

At 10 m thickness the borehole effect is negligible. In other words, the horizontal velocity data (p-wave potential) without the lens are the same as the pressure data with the lens. Figure 2.4 shows the horizontal particle-velocity data without the lens but receivers at the lens location. Similar observations can be made for a lens thickness of 5 m, 2.5 m, and 1 m as illustrated in Figure 2.5, and

Figure 2.6. These results suggest that the tube wave-like effect for boreholes located below the basalt layer is likely to be negligible or non-existent for horizontal boreholes.

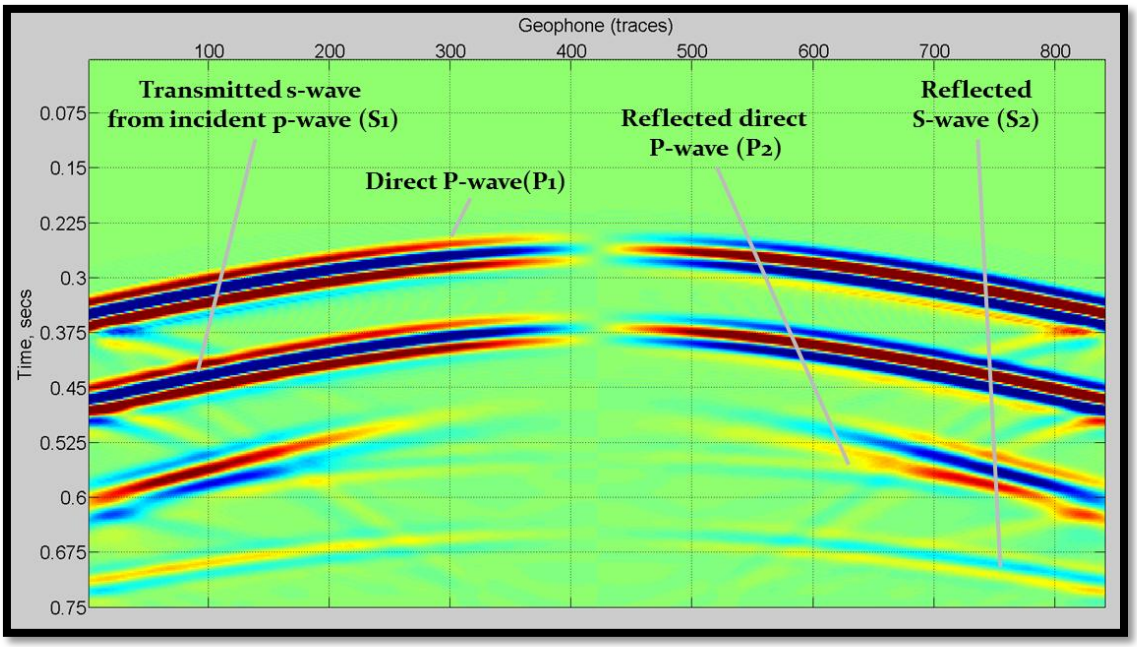

Figure 2.4. Borehole seismic data of geological construct in Figure 2.1 without the lens, physical quantity displayed is horizontal velocity data.

We should also note that at 10 m thickness, the lens is 20 times smaller than the wavelength in the basalt half-space. The 5 m-, 2.5 m-, and 1 m- thick lens was 38 times, 77 times and 192 times smaller, respectively, than the wavelength in the basalt layer. The grid-spacing modeling parameters were also different for each lens thickness; however, the time sampling and geological configuration remained the same. The grid spacing for the lens of thickness 5 m was 1 m, whereas for the lens of thickness 2.5 m, the grid spacing was 0.5 m. This change in the grid spacing will not change the borehole seismic data once the geological construct is maintained. The only effect we observe is the increased amplitudes of the boundary

reflected waves. Since the borehole-like seismic data remains consistent for different thicknesses, we will only consider a thickness of 2.5 m for the rest of the chapter.

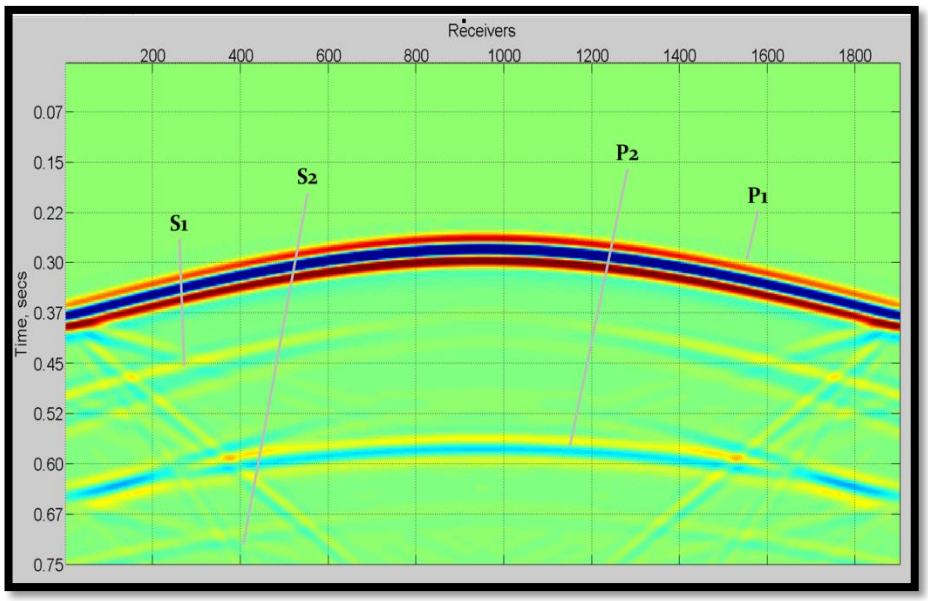

Figure 2.5. Borehole seismic data of geological construct in Figure 2.1 with lens of thickness 5 m, physical quantity displayed is pressure.

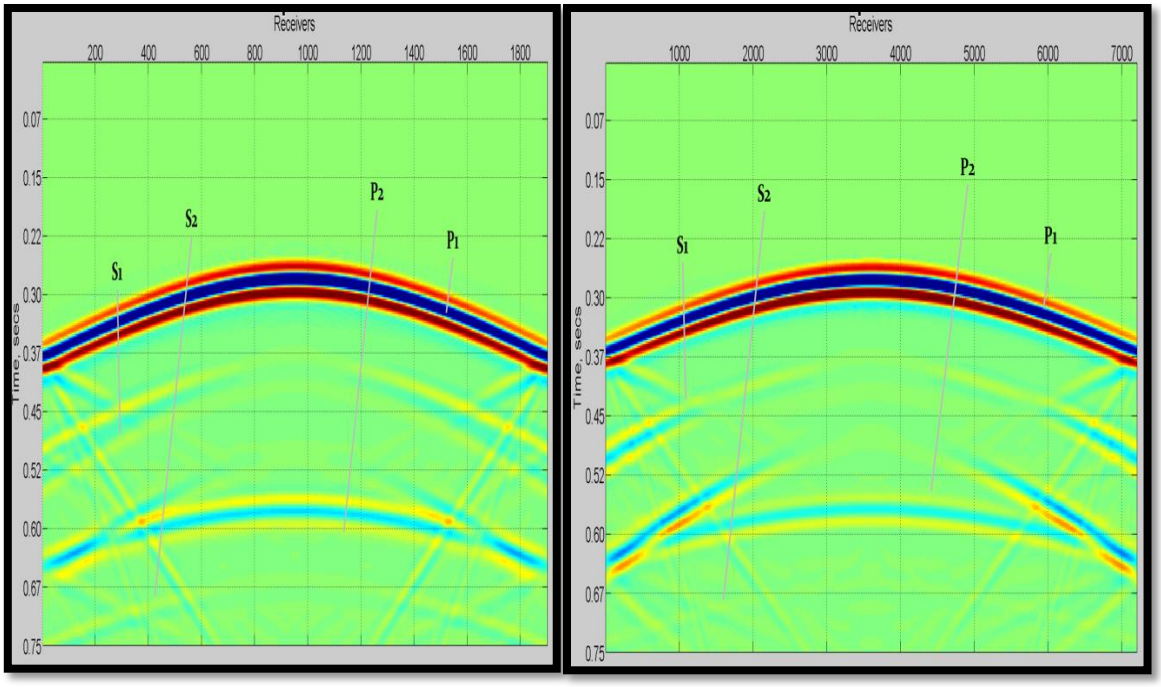

Figure 2.6. Borehole seismic data of geological construct in Figure 2.1 with lens of thickness 2.5 m (left) and thickness 1 m (right), physical quantity displayed is pressure.

The Effect of Borehole Geometry

The borehole below the basalt rocks is likely to be horizontal. The word *horizontal* in the borehole context is misleading because it includes boreholes with a dipping shape. All non-vertical borehole shapes are known in the borehole community as horizontal boreholes. So the lenses in Figure 2.1 and Figure 2.7 are both considered horizontal boreholes. The dipping borehole is needed in the case where the basalt layers containing hydrocarbons are dipping. In this case oil production is probably better optimized by using a dipping borehole. Figure 2.7 illustrates the dipping borehole with a thickness of 2.5 m.

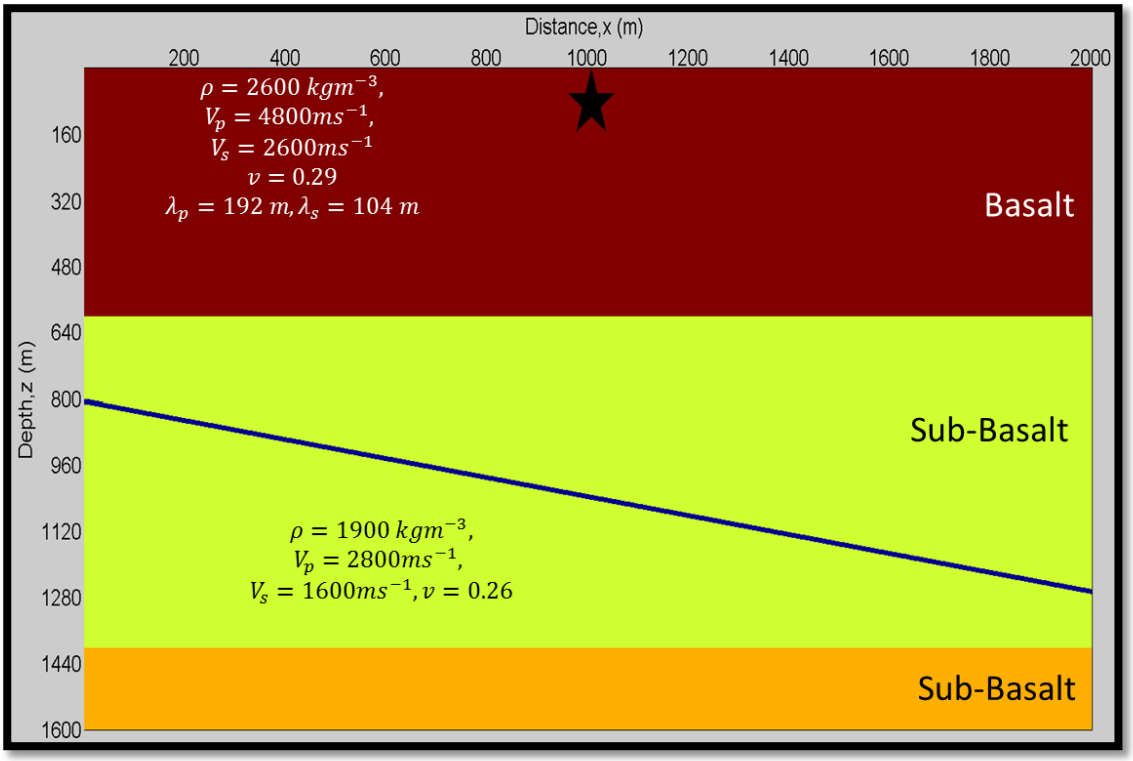

Figure 2.7. Geological construct of dipping lens, the source is represented by ★, where; ρ is density, V_p is velocity of the compressional wave, V_s is the velocity of the shear wave, v is the poisson ratio of the material, λ_p is the wavelength of the compressional wave and λ_s is the wavelength of the shear wave.

The corresponding data obtained from the finite difference are shown in Figure 2.8. The same modeling parameters were used in the case of the horizontal borehole of thickness 2.5 m.

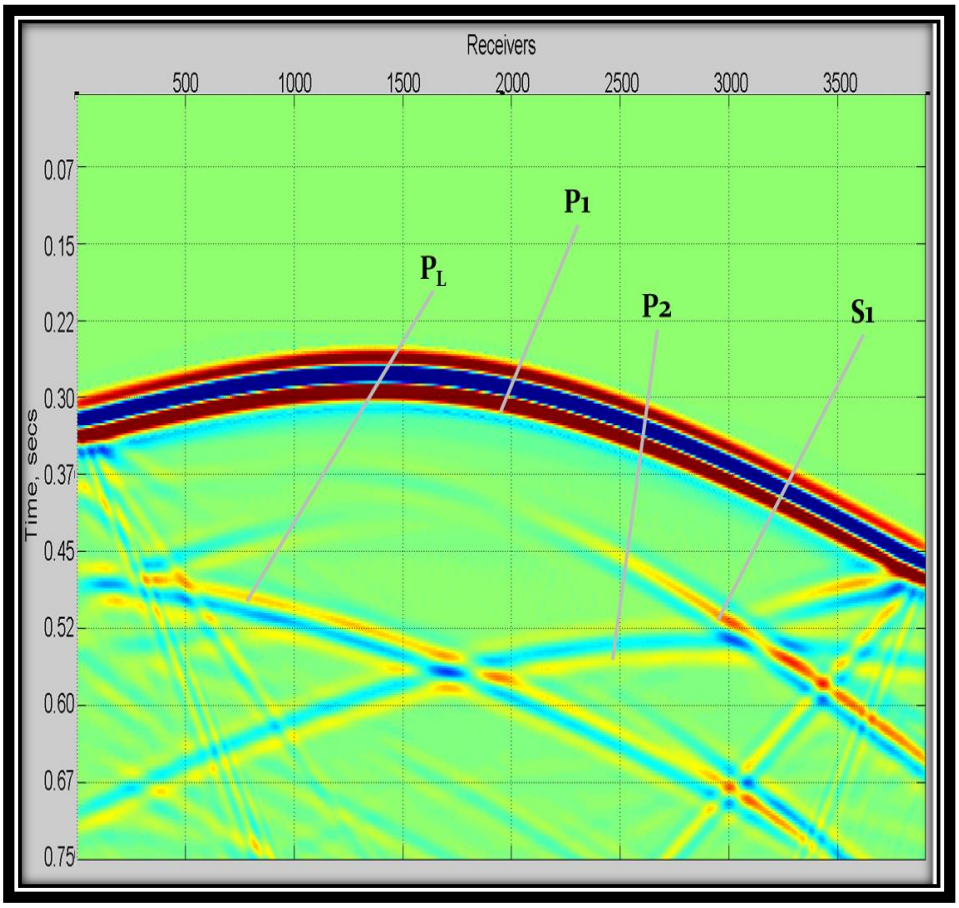

Figure 2.8. Borehole seismic data of geological construct in Figure 2.7 with dipping lense of thickness 10 m, physical quantity displayed is pressure.

At first glance the results can be interpreted as different from the borehole-like seismic data with strictly horizontal lenses. However, because of the dipping receivers, they have the same events except for the shape of these events. We will give a brief description of the additional events and prove how they are similar. The P_L event, as described earlier, is the reflection of the P_1 event from the lens, to the base of the basalt half-space then recorded by the receivers, as shown in Figure 2.3.

In the horizontal borehole-like seismic data shown in Figure 2.2, the P_L event is superimposed on the P_2 event. In the dipping-lens scenario, the travel-times for P_2 and P_L would be different. The P_2 event will be recorded in the deeper receivers

earlier than the P_L event, and vice versa for the shallow receivers. It should also be noted that the anomalous reflections at the extremes of the data are due to the ineffectiveness of the absorbing boundary conditions.

As expected, the results drawn from the previous exercise based on horizontal borehole in Figure 2.2 are also valid here. In other words, in this case the tube-wave effect on borehole seismic data is negligible.

Effect of Elastic Parameters on Borehole-like Seismic Data

The question that we are asking ourselves in this section is whether the results obtained so far can hold for elastic parameters in the sub-basalt layer differing from the one in Figure 2.2. To answer this question, we have investigated two additional scenarios of sub-basalt layers. We will start by looking at the results for a sub-basalt layer with low elastic parameters relative to the one shown in Figure 2.2. The geological construct is shown in Figure 2.9. These low elastic parameters can be caused by over-pressure shale below the basalt layer.

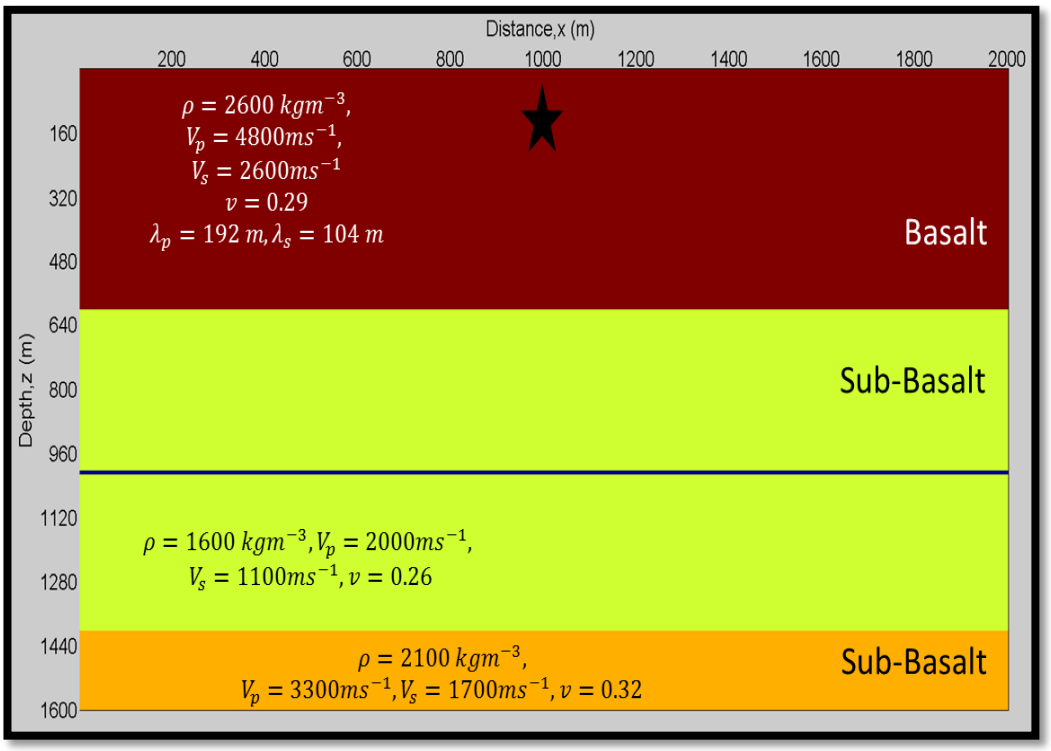

Figure 2.9. Geological construct of low elastic parameters relative to Figure 2.1 in the sub-basalt layer for a strictly horizontal lens of thickness 2.5 m.

The corresponding data obtained from finite-difference modeling are shown in Figure 2.10. The modeling parameters used were the same as those shown in Figure 2.2, except that the time for recording was increased by 100 ms to facilitate the larger travel times corresponding to the low velocities. The corresponding borehole-like seismic data for a dipping borehole are also shown in Figure 2.11.

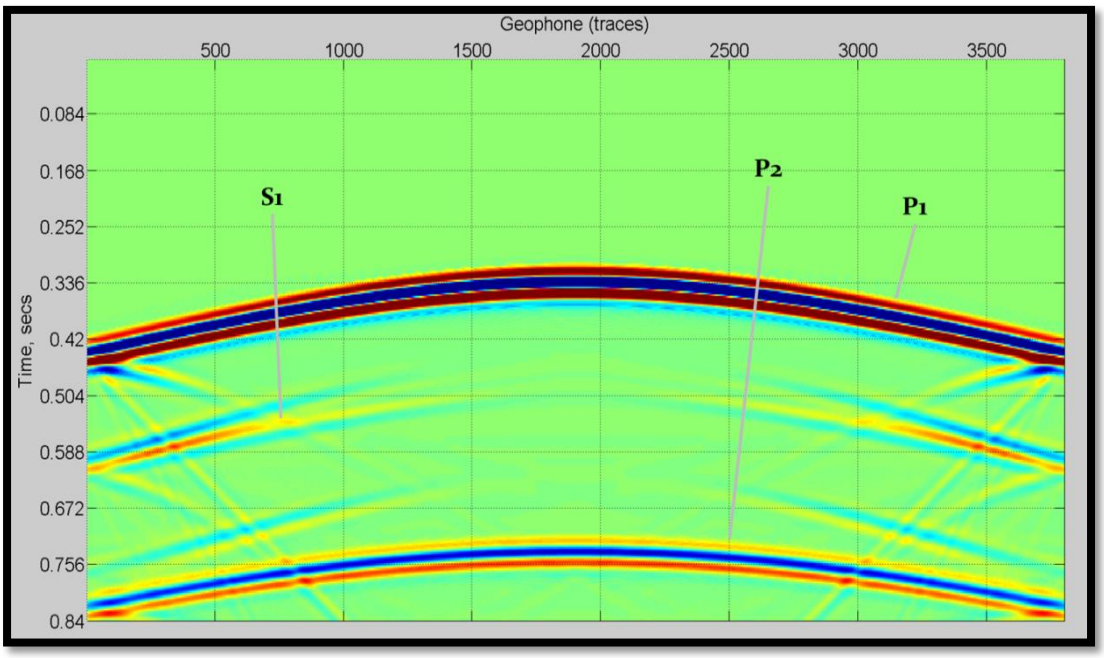

Figure 2.10. Borehole seismic data of geological construct in Figure 2.9 with lens of thickness 2.5 m, physical quantity displayed is pressure.

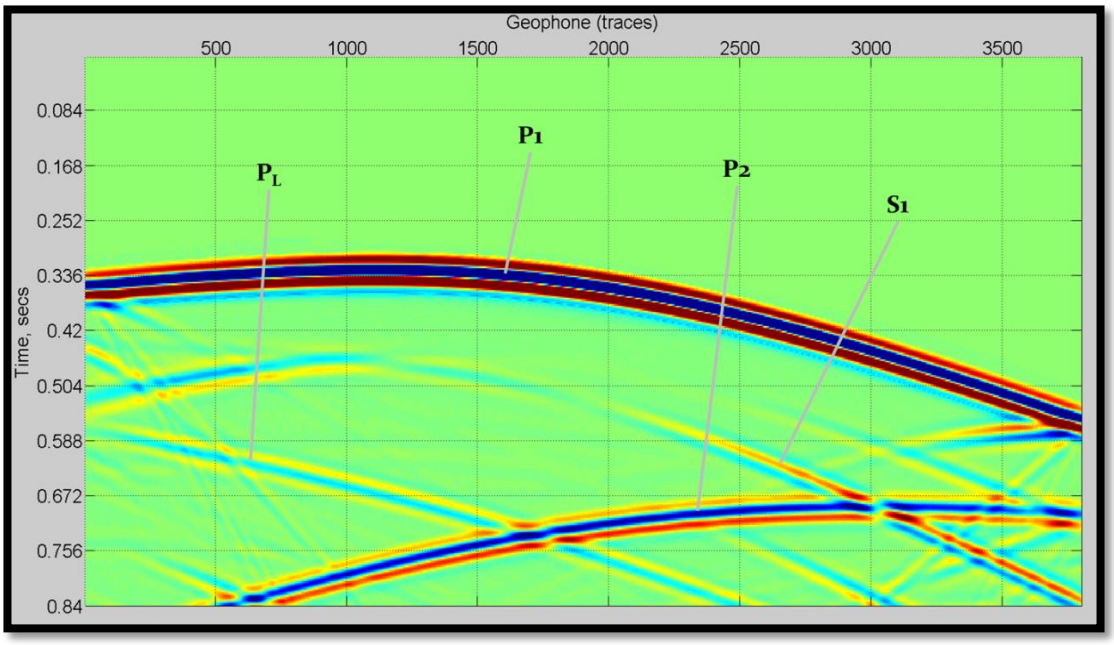

Figure 2.11. Borehole seismic data of geological construct in Figure 1.9, with dipping lens of thickness 2.5 m, physical quantity displayed is pressure.

We can see that the results stay consistent with the borehole seismic data given in Figures 2.1 and 2.8. However, as expected, the amplitudes of the events will differ because of the change in the impedance of the sub-basalt layer. The reflection coefficient between the basalt half-space and the sub-basalt layer is 0.6, whereas it is 0.4, for the lower half-space. Hence the reflected events (P_L and P_2) have higher amplitudes compared to the same events shown in Figure 2.2 and Figure 2.8. In this scenario the tube-wave effect on borehole seismic data is also negligible.

We will now look at a relatively high-acoustic-impedance sub-basalt layer compared to the one described in Figure 2.1. Figure 2.12 illustrates the geological construct for the dipping-lens example.

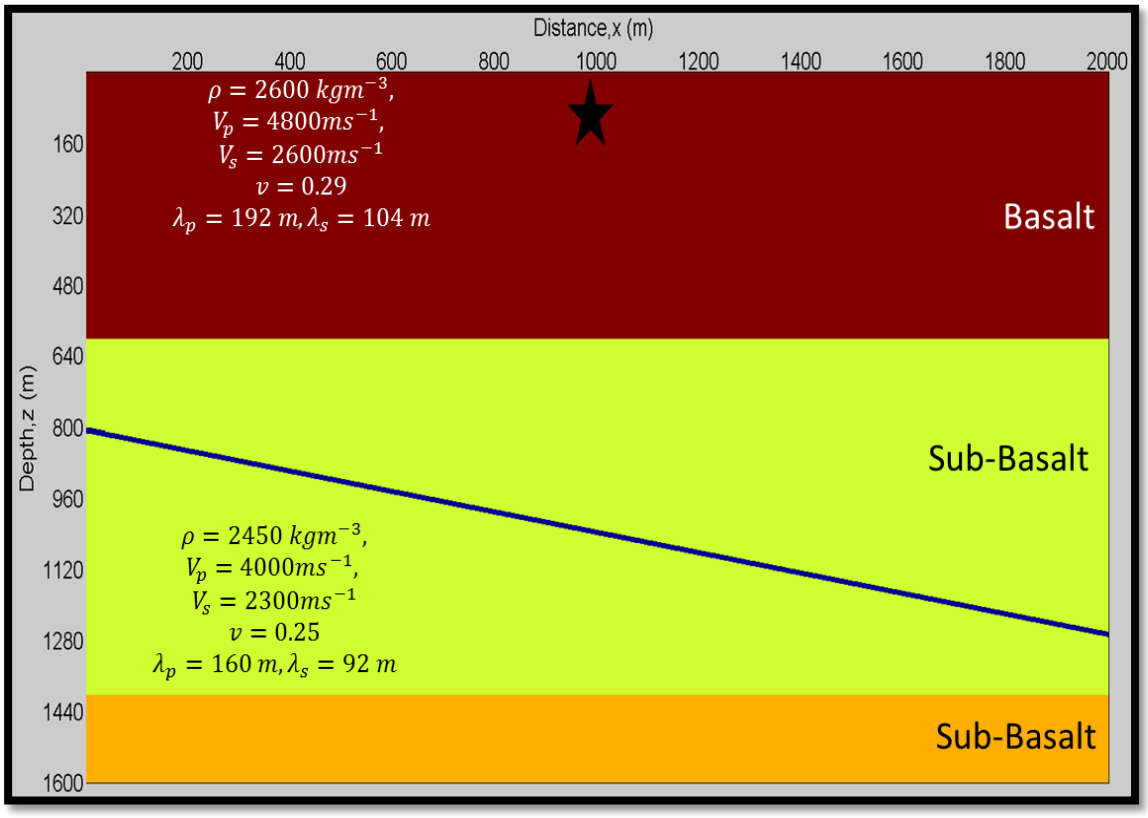

Figure 2.12. Geological construct of high elastic parameters relative to Figure 2.1 in the sub-basalt layer for a dipping lens.

The corresponding data obtained from the finite difference are shown in Figure 2.13 and Figure 2.14, for a horizontal lens and a dipping lens, respectively. The finite-difference modeling parameters used in Figure 2.2 are also used in this example.

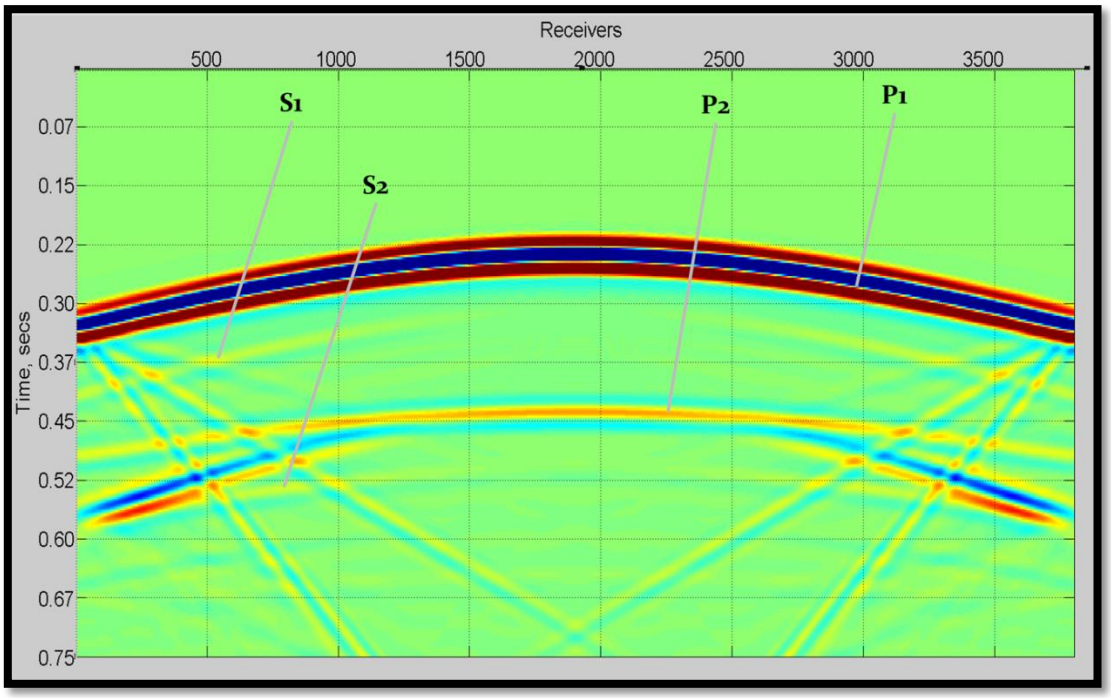

Figure 2.13. Borehole seismic data of geological construct in Figure 2.12 with horizontal lense of thickness 10 m, physical quantity displayed is pressure.

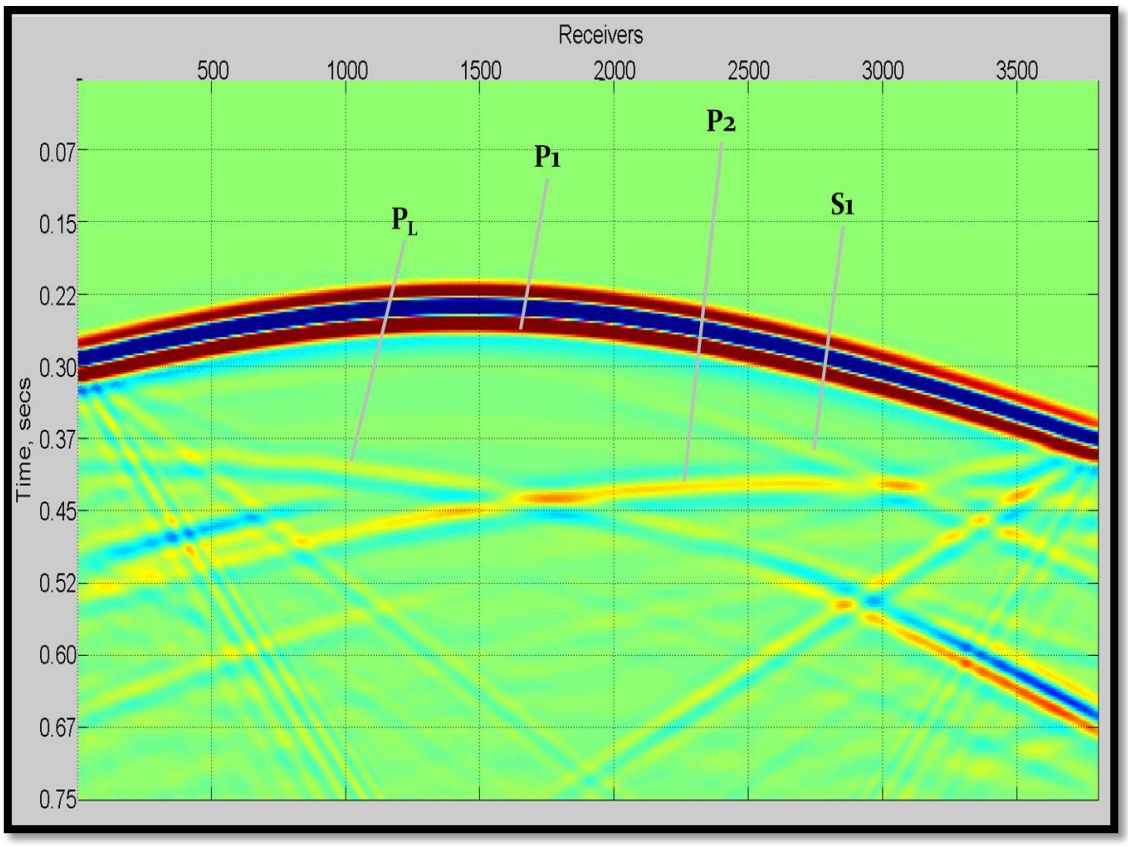

Figure 2.14. Borehole seismic data of geological construct in Figure 2.12 with dipping lense of thickness 2.5 m, physical quantity displayed is pressure.

As expected, we obtained relatively small amplitude reflections for P_2 and P_L events as compared to those shown in Figure 2.2 and Figure 2.8. Because the reflection coefficient between the basalt half-space and the sub-basalt layer is 0.1, whereas it is 0.2 for the lower half-space. However, we can see that the result stays consistent apart from the amplitudes in Figure 2.2. Therefore we conclude that the tube-wave effect is negligible in this case.

So far we have not included the wash-out zone in any of our models. This case will now be discussed.

Effect of the Wash-out Zone on Borehole-like Seismic Data

Wash-out zones are areas where the borehole thickness increases. Generally washout zones in the borehole can give rise to tube-waves. In our study the wash-out zone is modeled as a lateral extension of the lens, as shown in Figure 2.15. In this section we populated half of the lens with four wash-out zones at receivers 50, 150, 250, and 350. The wash-out zone laterally extends 0.5 m (one-fifth the size of the lens) and spans 10 m along the lens which is four times the diameter of the lens.

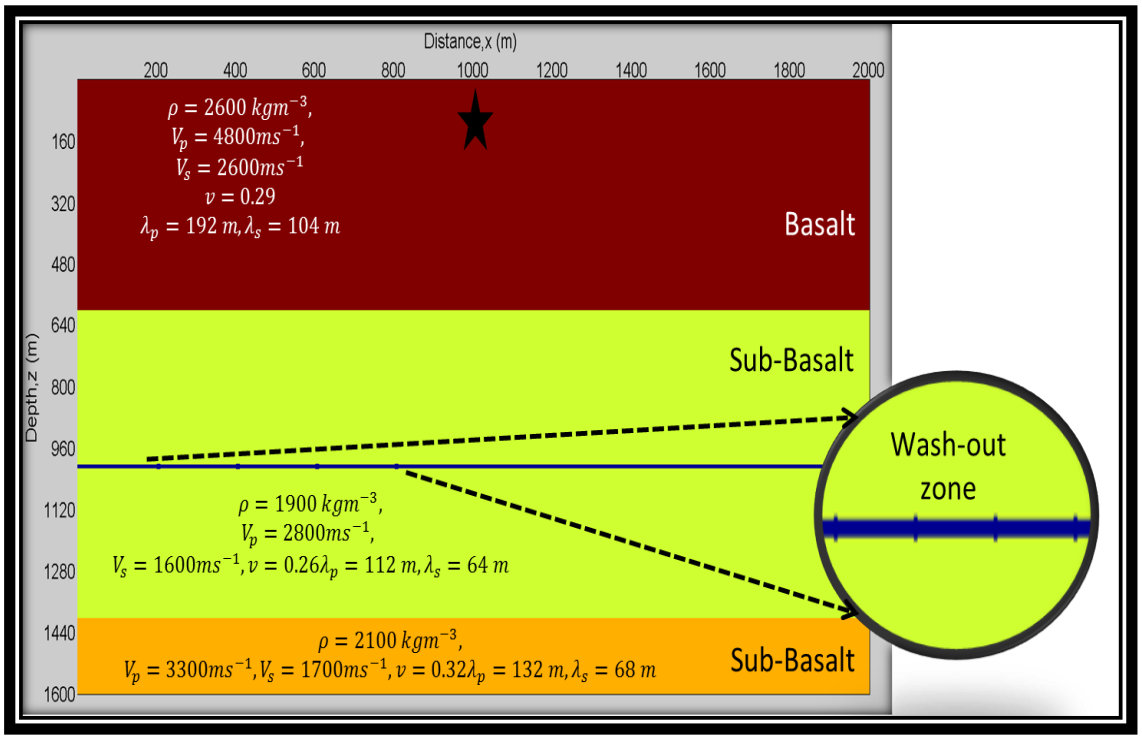

Figure 2.15. Geological construct of wash-out zone along the lens of thickness 2.5 m in the sub-basalt layer.

The corresponding data obtained from the finite difference are shown in Figure 2.16. The finite-difference modeling parameters used in Figure 2.2 are also used in this example.

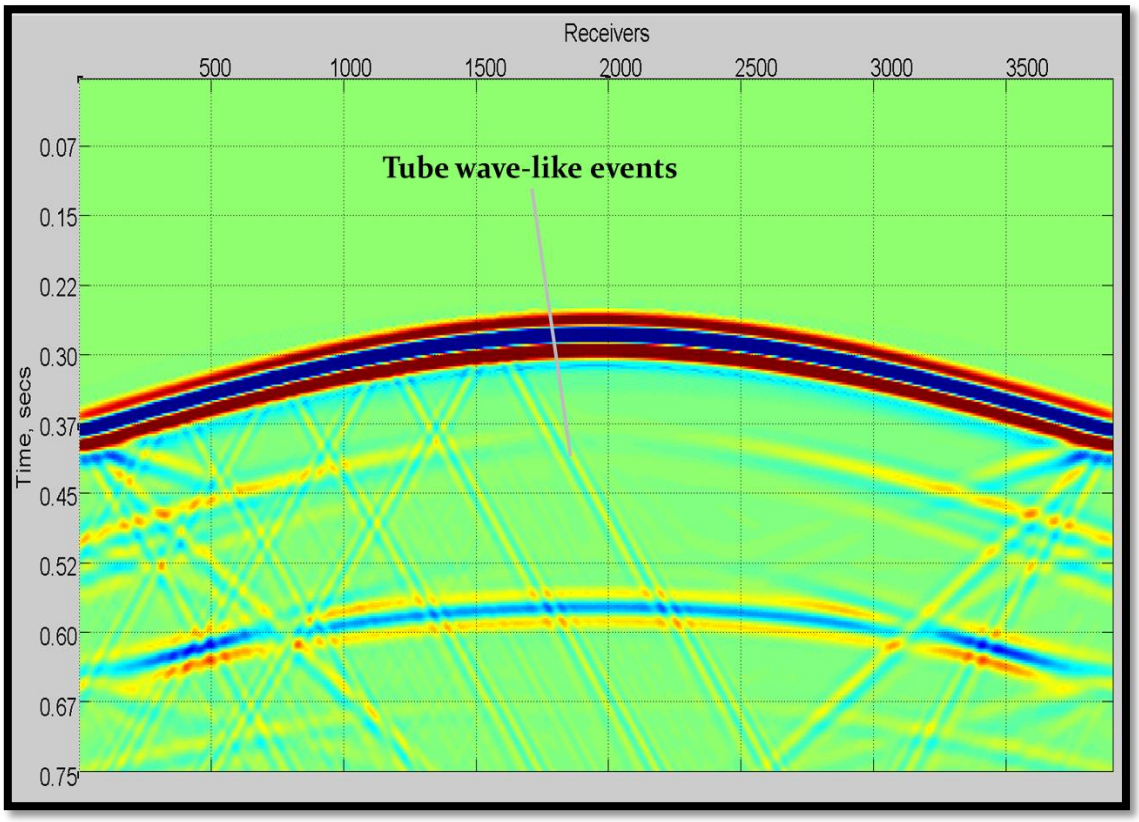

Figure 2.16. Borehole seismic data of geological construct in Figure 2.15; a horizontal lens with wash-out zones that spans five times the size of the lens.

The reflection events in the borehole-like seismic data remain consistent with Figure 2.2, except now we also have the generation of tube wave-like events. These tube wave-like events have a velocity less than the fluid in the lens for this model. In an uncased borehole, the tube wave velocity is never greater than the velocity of the fluid in the borehole. In this example we calculated the tube wave

velocity to be approximately 1000 ms^{-1}. Also we observed the effect of the boundary reflecting waves back into the medium instead of perfectly absorbing them. We also considered the case where the wash-out laterally extends 0.5 m (one-fifth the size of the lens) and spans 2.5 m along the lens which is the same diameter of the lens. The borehole seismic data is illustrated in Figure 2.17.

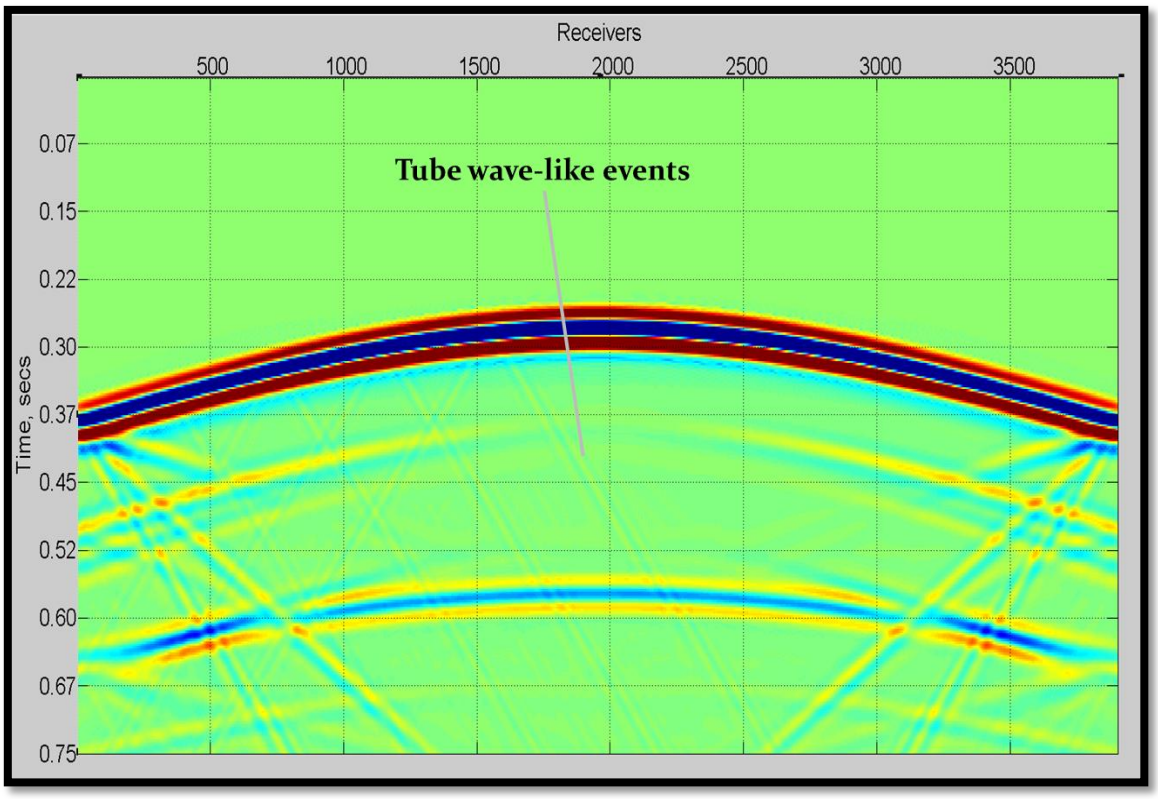

Figure 2.17. Borehole seismic data of geological construct in Figure 2.15; a horizontal lens with wash-out zones that spans one time the size of the lens.

We will also consider this effect in a dipping borehole in the sub-basalt layer. The corresponding borehole-like seismic data are shown in Figure 2.18. Again the reflection events remain consistent with what is seen in Figure 2.9; however, the wash-out zone introduces these tube wave-like events. These tube wave-like events remain consistent with the borehole-like data observed in the horizontal lens with

wash-out zones example. We can therefore conclude that we may expect to see on borehole seismic data these tube-wave events in more realistic models of ultra-deep waters.

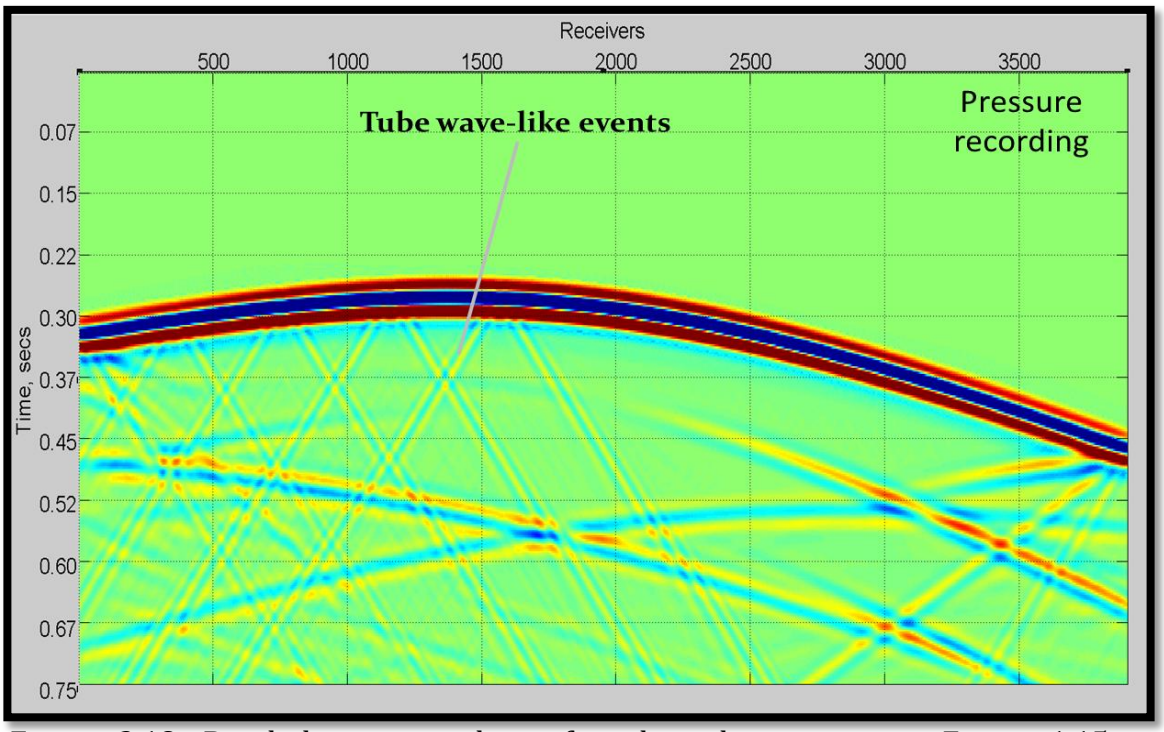

Figure 2.18. Borehole seismic data of geological construct in Figure 1.15; a horizontal lense with wash-out zones.

It should be noted that in most if not all the borehole seismic data, that there were reflections from the boundaries. Therefore the events close to the edges of the data should be neglected.

CHAPTER III

A CONSTRUCTION OF GEOLOGICAL MODELS FOR ULTRA-DEEP WATERS

The geology of ultra-deep-water regions is very complex. In this chapter we will discuss these complexities. We will discuss particularly the size of the water column, the topography of the sea floor, the interfaces of the basalt layer, and the structure of heterogeneities within the basalt layer. We will also construct two geological models for ultra-deep-water regions similar to the Mid-Norway Basin and the Northwest Australian Basin.

We will start with the definition of ultra-deep water and deep water in the geophysical literature. The scheme adopted in this thesis is the definition used in petroleum seismology. Figure 3.1 illustrates this classification.

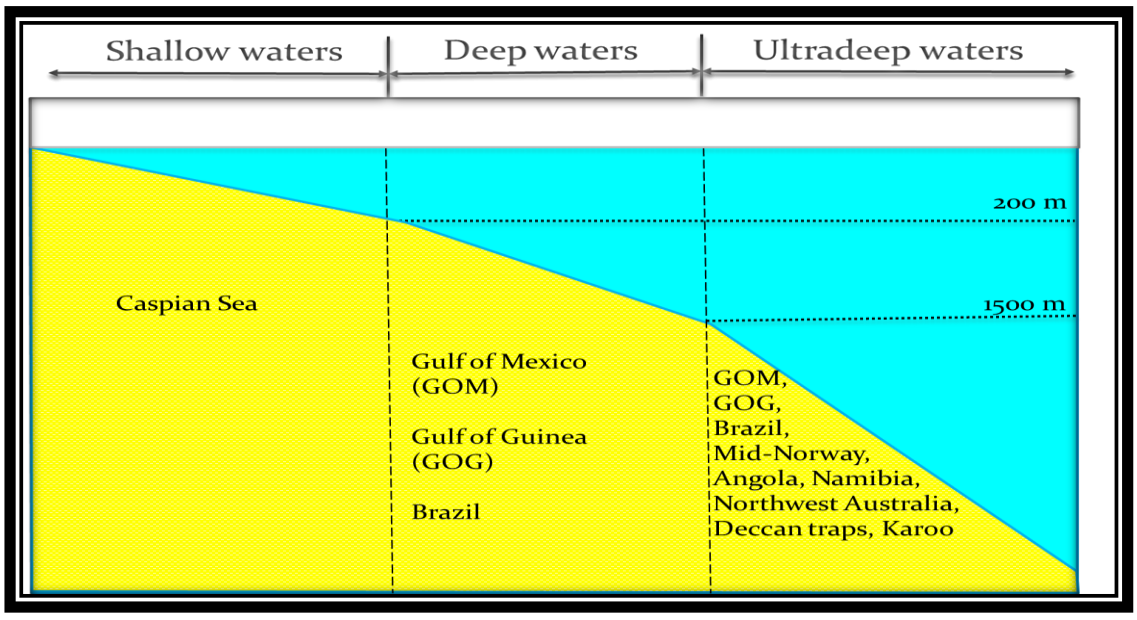

Figure 3.1. Shows the classification of ultra-deep water, deep water and shallow water.

- Deep water: water depth greater than 200 m (656 ft) but less than 1500 m (4921 ft)
- Ultradeep water: water depths greater than 1500 m (4921 ft)

On Figure 3.1, we have also illustrated some of the basins around the world that are present hotspots for hydrocarbons exploration. Of these basins in ultra-deep waters, the Mid-Norway basins, Angola basin, Namibia basin, Karoo basin, Deccan Traps and the Northwest Australian basin have reservoirs located below basalt layers. We will now describe how we modeled ultra-deep waters and the associated geology.

Figure 3.1, defines the first characteristic of our ultra-deep-water geological construct—i.e. the depths at which we have ultra-deep water. In our model, the sea floor was simulated as a seaward dipping interface ranging from a depth of 1600 m to 2000 m. In this environment the sea floor has gently undulating and non-flat characteristics that are observed in seismic data offshore mid-Norway (GeoExpro 2011).

In ultra-deep water, extensive basaltic lava flows were produced during continental breakup and flowed across pre-breakup sedimentary basins (White and McKenzie, 1989). These rift basins can be structurally complex. For this reason, the overlying basalt sediment is normally faulted in our geological constructs of ultra-deep waters. In addition, the basalt layer in each of our geological constructs has high impedance with respect to the surrounding sedimentary layers and was about 400 m thick. In the following section we will construct the geological model for two basins:

1. The Voring and More basins off mid-Norway
2. The Northwest Australian Basin

Mid-Norway Basin-like Model

The Voring and More basins' basalt layer is characterized by a very a rough top and bottom surface (Singh, 2005). This type of basalt surface is also present in parts of the Greenland basins. The rough top and bottom surface of the basalt can cause significant scattering and absorption of seismic energy, both of which can severely distort imaging of sub-basalt layers. Rough surfaces can also have a detrimental effect on the signal-to-noise ratio. The ultra-deep water mid-Norway-type model is illustrated in Figure 3.2.

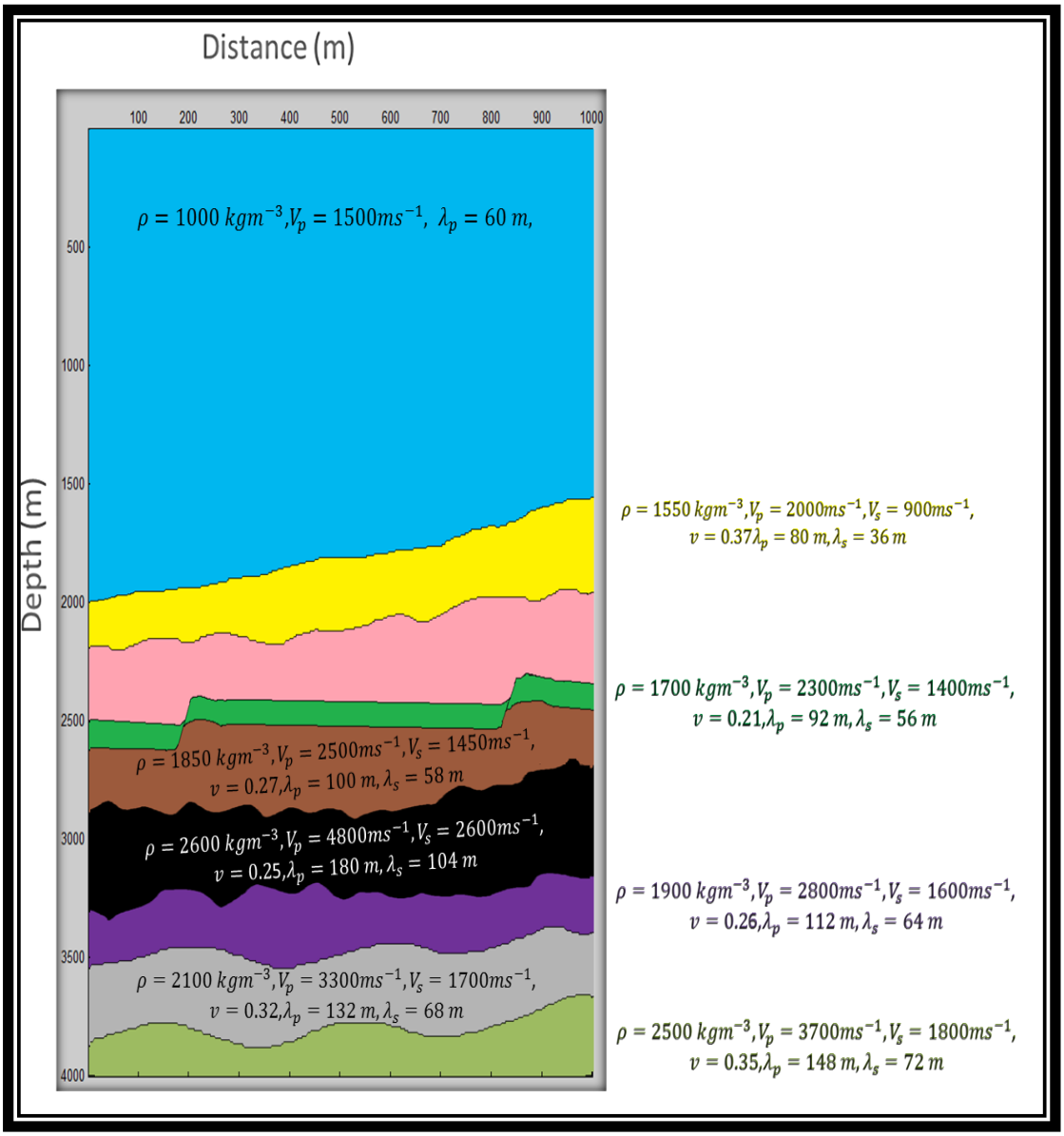

Figure 3.2. Illustrates the ultra-deep waters geological construct for a non-smooth top and bottom basalt surface (Mid-Norway-like Model); ρ is density, V_p is velocity of the compressional wave, V_s is the velocity of the shear wave, v is the poisson ratio of the material, λ_p is the wavelength of the compressional wave and λ_s is the wavelength of the shear wave.

Northwest Australian Basin-like Model

Basalt layers can be heterogeneous volcanic rock characterized by vertically and laterally varying velocities and irregular interfaces (Martini et al. 2005). The Northwest Australian Basin basalt layer is characterized by small-scale heterogeneities such as the presence of trapped bubbles (vesicular basalt) (Singh, 2005), as seen in Figure 3.3.

This phenomenon forms when rising magma intrudes the overlying sedimentary layers, comes to the surface and rapidly cools. Consequently the gases in the magma do not have sufficient time to be expelled and are trapped within the basalt rock. These small-scale heterogeneities are modeled in our Australian basin-type geological construct. The Karoo Basin in South Africa is also known for such heterogeneities within the basalt layer.

The model given in Figure 3.3, has the same geology as in Figure 3.2, however just the basalt layer differs.

Therefore the borehole-like data which we will analyze in the next chapter will be the irregular top and bottom basalt surfaces similar to those in the Mid-Norway Basin and the small-scale heterogeneities within the basalt surface, similar to those in the Northwest Australian Basin.

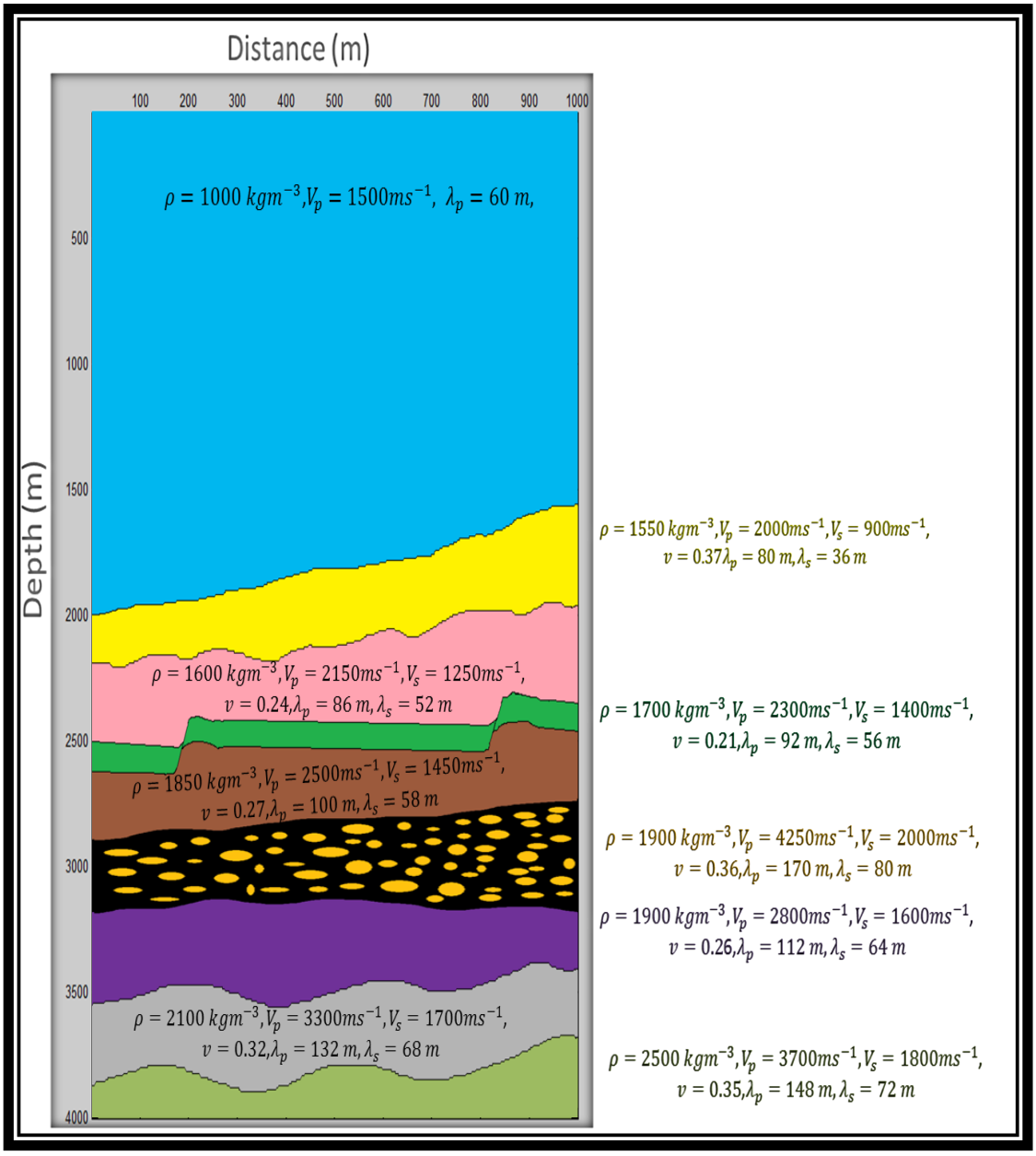

Figure 3.3. Illustrates the ultra-deep waters geological construct for a non-smooth top and bottom basalt surface (Australian Basin like Model); ρ is density, V_p is velocity of the compressional wave, V_s is the velocity of the shear wave, v is the poisson ratio of the material, λ_p is the wavelength of the compressional wave and λ_s is the wavelength of the shear wave.

CHAPTER IV

ANALYSIS OF BOREHOLE-LIKE DATA FOR ULTRA-DEEP WATERS

In this study we used a 2D staggered-grid finite difference. This algorithm imposed on us specific conditions and limitations. In this chapter we will briefly review the finite-difference method and discuss these conditions and limitations. We modeled ultra-deep-water regions in Chapter III; we will now study wave propagation below the basalt layer using these models—i.e., the Mid-Norway basin-like model and the Northwest Australian basin-like model. These data will be recoded as borehole seismic data.

A Brief Review of the Finite Difference Method

The finite-difference technique is by far the most accurate tool for simulating elastic wave propagation when an adequate discretization in space and time is possible. This method gives an accurate computation of derivatives of the wave equation (Ikelle and Amundsen 2005). A detailed description of finite difference is discussed in Appendix A. In this section we will discuss how we used the finite- difference method and what limitations and conditions it imposed on us.

The basalt layer in ultra-deep waters are laterally varying, therefore a 3D geologic model should be used to model these lateral heterogeneities. Therefore, we should also propagate 3D waves from a point source. The borehole which is placed below the basalt rocks should be modeled as a cylindrical tube of diameter about 0.1 m. However available to us was a 2D finite difference. Therefore our geological model was 2D, we propagated 2D waves into our model and our borehole was simulated as an acoustic lens of thickness 2.5 m. The acoustic lens is a thin layer filled with water that is laterally infinite. Therefore, the lens may not adequately model the waves that propagate in the cylindrical coordinates. In

addition, unlike the borehole, the lens will act like a plane and reflect and refract seismic waves.

Another limitation of the finite-difference algorithm is grid dispersion. This error exists because of the truncation that we make when we approximate the spatial derivatives (Ikelle and Amundsen, 2005). In this study we approximated the spatial derivatives by a fourth-order approximation (given in Appendix A). This approximation requires a minimum of five grid points per wavelength (Levander, 1988). We used equation 1 (Levander, 1988), to ensure that we did not violate the gird dispersion.

$$\Delta x < \frac{V_{min}}{5 f_{max}} \quad \ldots (1)$$

To ensure accurate wave-propagation simulation in the lens, the lens thickness was modeled with at least five grid points. Therefore, to realistically model the borehole, which can have a diameter of 0.1 m, the grid size, Δx, needs to be 0.02. In our models the vertical depth of the ultra-deep environment is 4000 m. Therefore 200,000 grids are needed to effectively model the vertical depth. This large number of grids would require computational resources beyond what is available to us. Hence, in this study the lens for the ultra-deep-water models were 10 m thick.

In addition, the recursive computation used to solve the set of finite-difference equations can be numerically unstable. This instability occurs when we violate the following condition given in equation 2, (Levander, 1988):

$$\Delta t < 0.606 \frac{\Delta x}{V_{max}} \quad \ldots (2)$$

Equation (2) implies with large V_{max} (4800 ms^{-1}) and small Δx; the amount of time steps to model ultra-deep waters realistically will be to0 large and therefore beyond our computational abilities. Hence, we used a Δx of 2 m, which

corresponded to a satisfactory Δt of 0.25 ms (which is within the stability conditions).

Finite-difference modeling also requires discretization of space. In other words, the model is constructed using square grids. Therefore curved or dipping surfaces are not perfectly smooth. The roughness of these surfaces creates artifacts on the seismic data. This effect was observed in Chapter I for the dipping lenses. This effect can be minimized by using a relatively small grid size compared to the wavelength. The range of grid sizes that gives satisfactory results for the dipping lenses was 2 m or less for the basalt and sub-basalt layers, which corresponds to 96 times the dominant wavelength.

In our study we applied an absorbing boundary condition around the model. Numerically this condition is not perfectly absorbing; as a result there can be some residual reflection events from these boundaries. Although this event may normally be negligible, in our case it was not. The small-amplitude events that were recorded on the bore-like seismic data in Chapter II had to be boosted for viewing due to the difference in impedances. The boost resulted in negligible reflections from the boundary being visible and hence created artifacts on the borehole-like seismic data.

Model I: Data for Mid-Norway Basin-like Model

In this section we considered a horizontal lens of thickness 2.5 m in the sub-basalt layer for the mid-Norway-like ultra-deep-water model, as shown in Figure 4.1. The explosive source is positioned in the water column with a central frequency of 25 Hz, which corresponds to a wavelength of 60 m. The receivers were placed inside the lens, and then the pressure was measured.

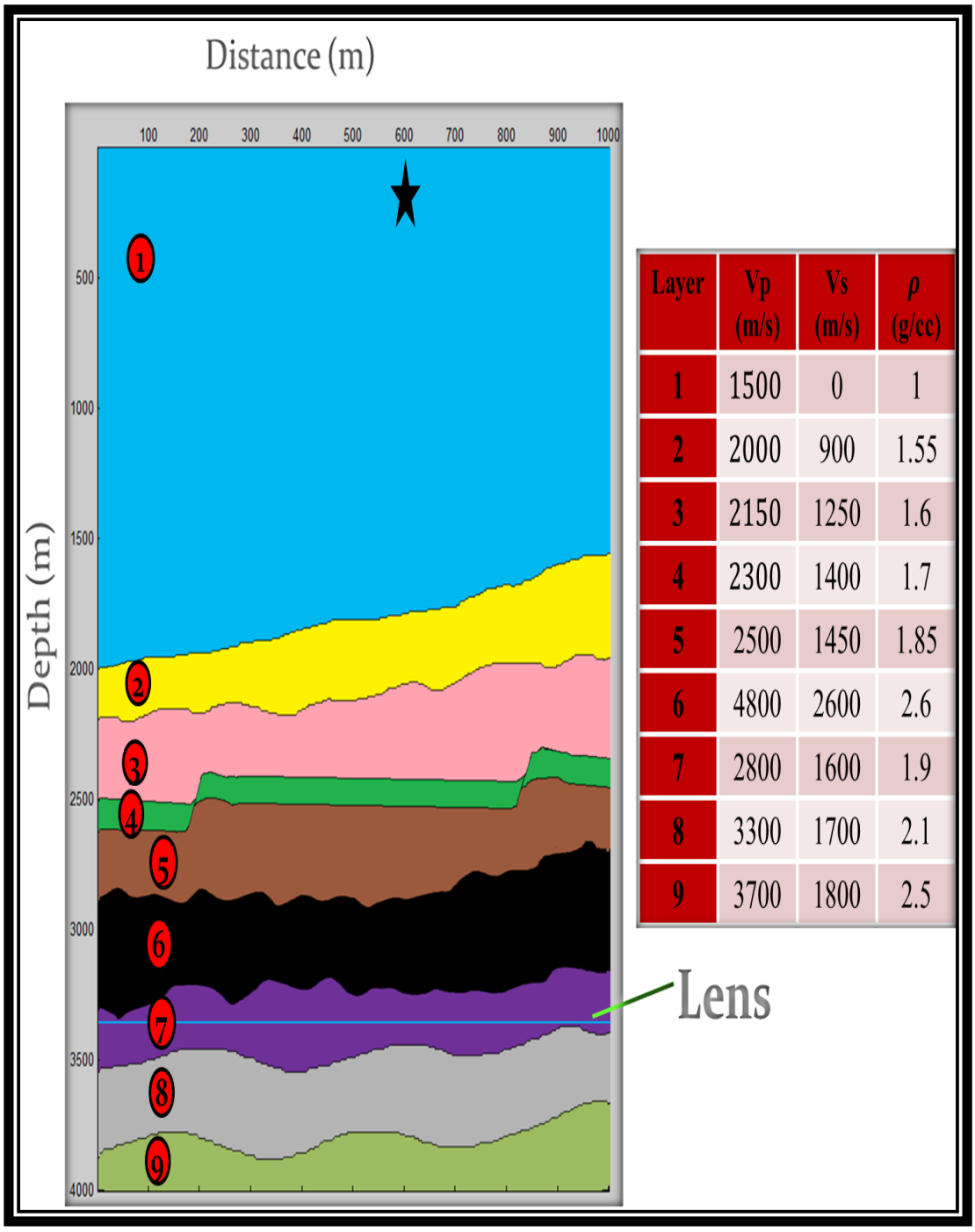

Layer	Vp (m/s)	Vs (m/s)	ρ (g/cc)
1	1500	0	1
2	2000	900	1.55
3	2150	1250	1.6
4	2300	1400	1.7
5	2500	1450	1.85
6	4800	2600	2.6
7	2800	1600	1.9
8	3300	1700	2.1
9	3700	1800	2.5

Figure 4.1. Geological construct of Mid-Norway-like model with lens in the sub-basalt layer; the associated elastic parameters for each layer is given to the right.

The associated borehole seismic data are shown in Figure 4.2 and Figure 4.3. The modeling parameters included a time sampling of 3.9 ms and grid size of 0.5 m. The receivers recorded pressure inside the horizontal lens. In this section, the data were clipped to show the receiver recordings below the basalt layer. These receivers in the lens measured pressure.

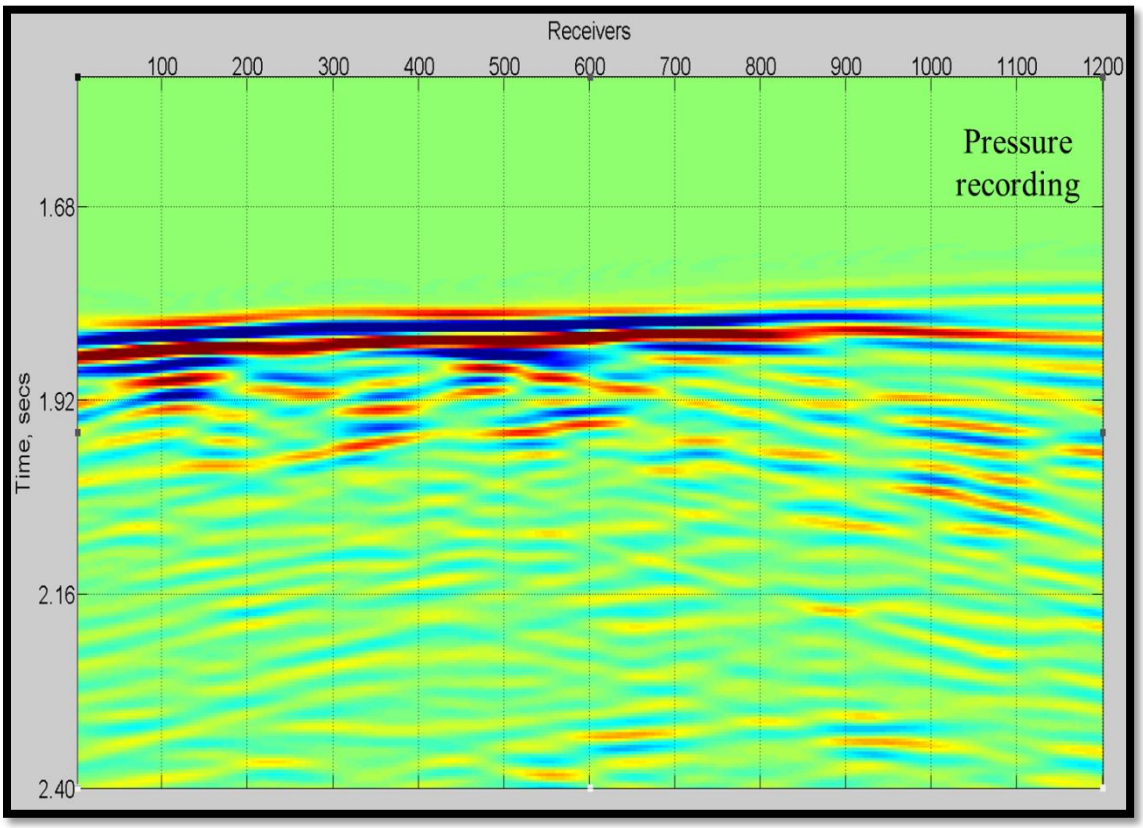

Figure 4.2. Borehole-like seismic data for horizontal lens positioned in the sub-basalt layer for the Mid-Norway-like model; without interpretation.

Figure 4.2 is a recording of pressure. We can observe that the incoming seismic waves were recorded after 1.8 seconds. The length of the borehole seismic data was 600 m. On this raw seismic data we can see possible events which may be associated with reflections from the sub-basalt layers and internal multiples. The finite difference technique allows us exactly locate where the positions of the sub-basalt layers will be located; this interpretation is shown in Figure 4.3.

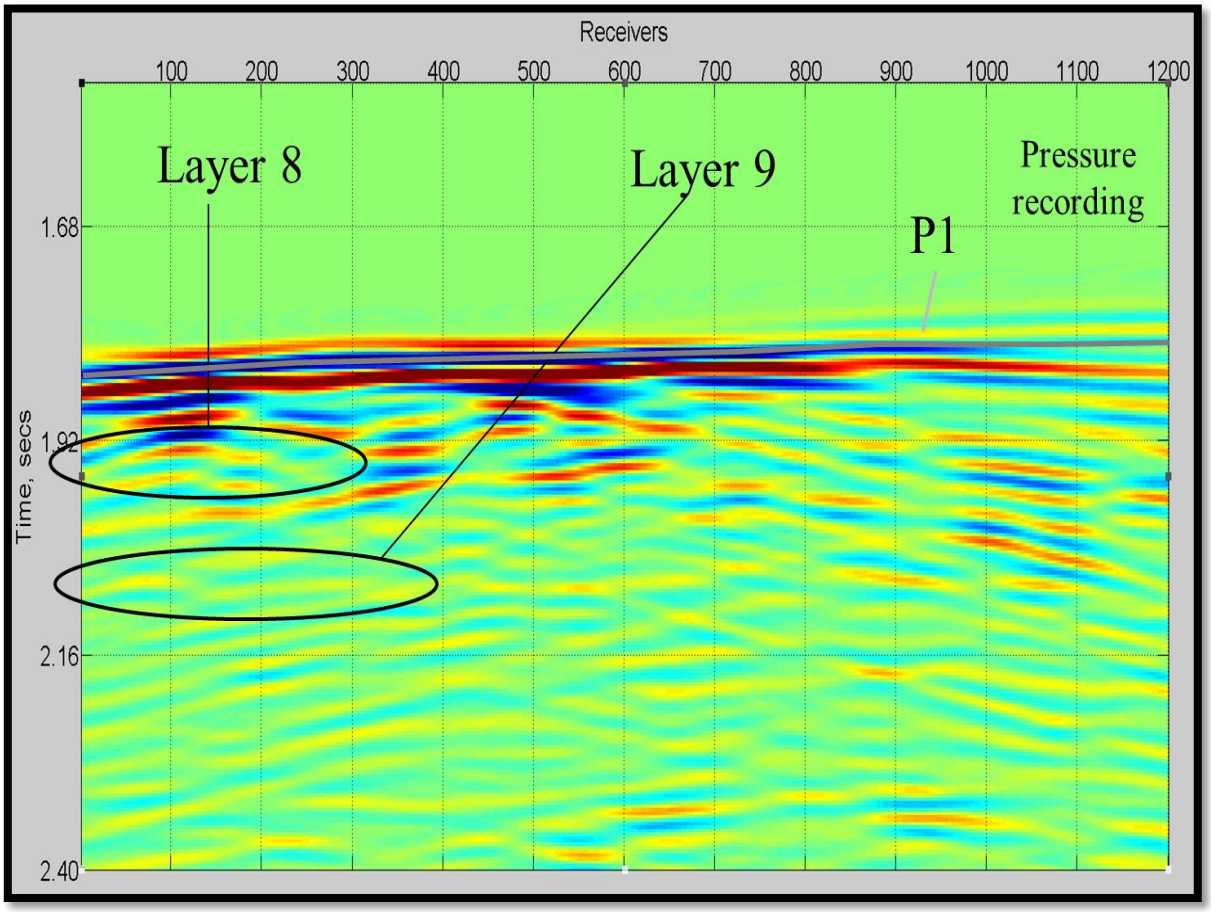

Figure 4.3. Interpreted borehole-like seismic data for horizontal receivers positioned in the sub-basalt layer for the Mid-Norway-like model.

On Figure 4.3, as expected, the direct arrival was sea-ward-dipping, since the sea floor was seaward-dipping. To identify the location of the top of layer 8 and layer 9 would have been difficult without the FDM technique. There were many reflections that looked like possible sub-basalt layer reflections however these were actually internal multiples. Also seen on our data, was diagonal events projecting outwards from around the 500th receivers, these events were interpreted as scattered events from the rough top and bottom surface of the basalt layer.

To interpret the top of layer 8 and layer 9 across the data is not possible. This is because these events we weak and were also masked by the internal multiples within the data and reflections from the lens. Layer 9 had smaller amplitudes than layer 8 because less energy propagates lower down. Hence we concluded that imaging below the basalt layer using borehole seismic data was poor for Model I.

We will now consider borehole seismic data for the lens with heterogeneities located sub-basalt, i.e. wash-out zones, Figure 4.4. The wash-out zones were placed at the 200th, 600th and 1000th receiver locations. The wash-out zone was modeled as a lateral extension; two fifths the size of the borehole. The length of the washout zone is four times the size borehole.

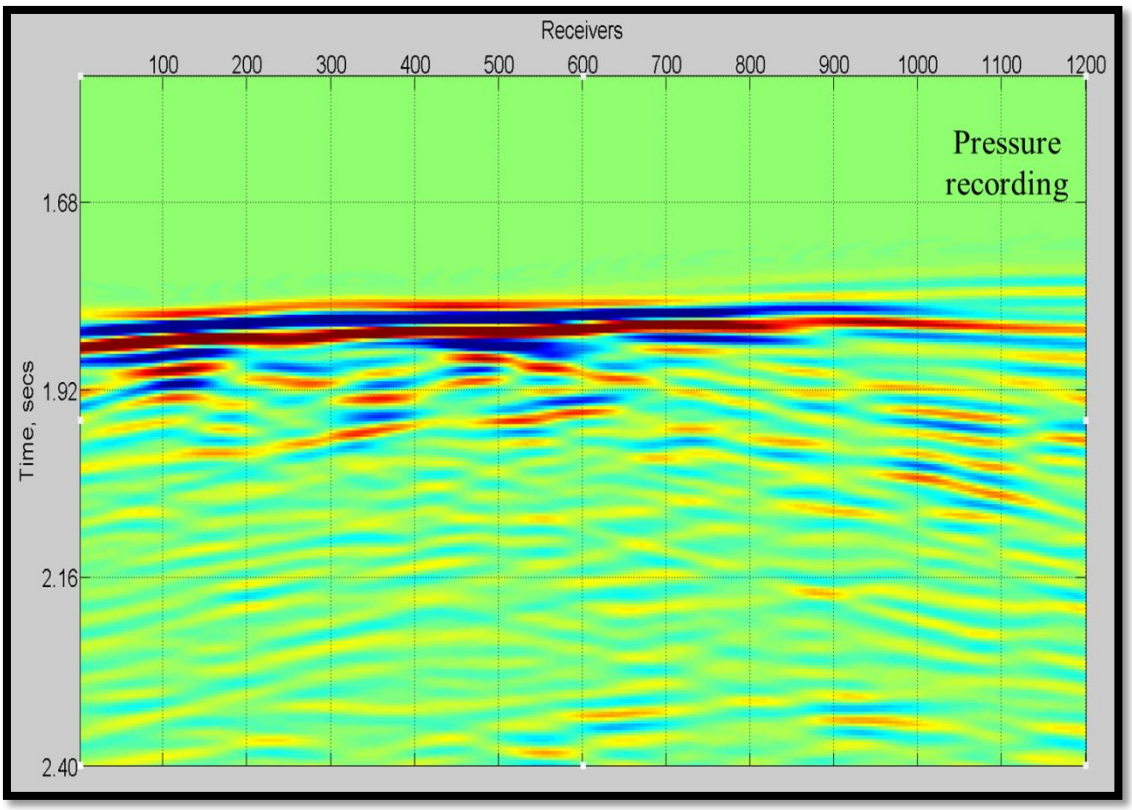

Figure 4.4. Borehole-like seismic data for horizontal lens with wash-out zone positioned in the sub-basalt layer for Mid-Norway-like model.

Figure 4.4 does not have any visible, characteristic upside down 'V' shape events at the wash-out zones i.e. there are no tube waves seen on the data. The lack of any visible tube waves were attributed to the limited energy that propagated in the sub-basalt layers and the relatively large wavelength, 196 times bigger than the wash-out zone, in the sub-basalt layer. There were, however, events cross-cutting the data, similar to the effect of tube waves, as shown in Figure 4.4. However, these velocities were far higher than the velocity of the fluid in the lens (1500 ms^{-1}) and therefore could not have been the tube wave-like events, as shown in Chapter II. Also, the cross-cutting effect was also observed on the borehole-like seismic data with lens, hence confirming these events are not tube waves. The interpreted borehole seismic data with the wash-out zones are shown in Figure 4.5.

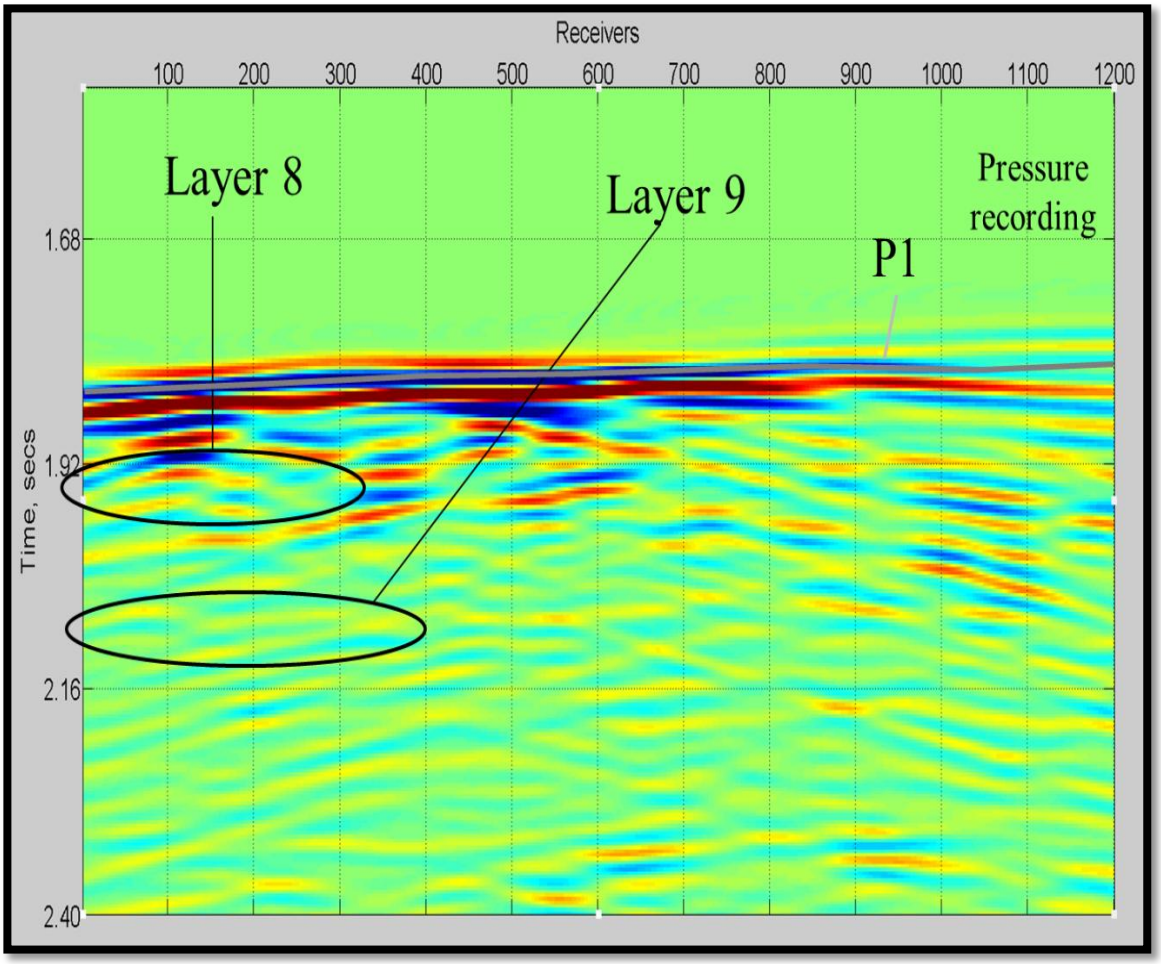

Figure 4.5. Interpreted borehole-like seismic data for horizontal lens with washout zones located in the sub-basalt layer for the Mid-Norway-like model.

Model II: Data for Northwest Australian Basin-like Model

In this section we consider a horizontal lens. The geological construct of the Ultra-deep water model with the lens is shown in Figure 4.6. The modeling parameters were the same as in the previous horizontal lens in the Mid-Norway basin-like model. The source is also placed in the water column at the 600 m mark. The source has a central frequency of 25 Hz, which corresponds to a seismic wavelength propagating from the basalt layer into the sub-basalt layer of 192 m.

In this model, the lens is 2.5 m thick and positioned below the basalt layer. The grid size for our model is 0.5 m. Some may ask why we didn't put the thickness of the lens as 0.5 m. The reason for the lens being 2.5 m thick is that to properly model wave propagation inside the lens we need at least four grid points.

We need at least four grid points because the finite difference method is an averaging program. So the more grid points we use to average wave propagation the better our results will be. This is discussed in Appendix A. Hence one grid point will not give accurate results compared to five grid points which corresponds to 2.5 m.

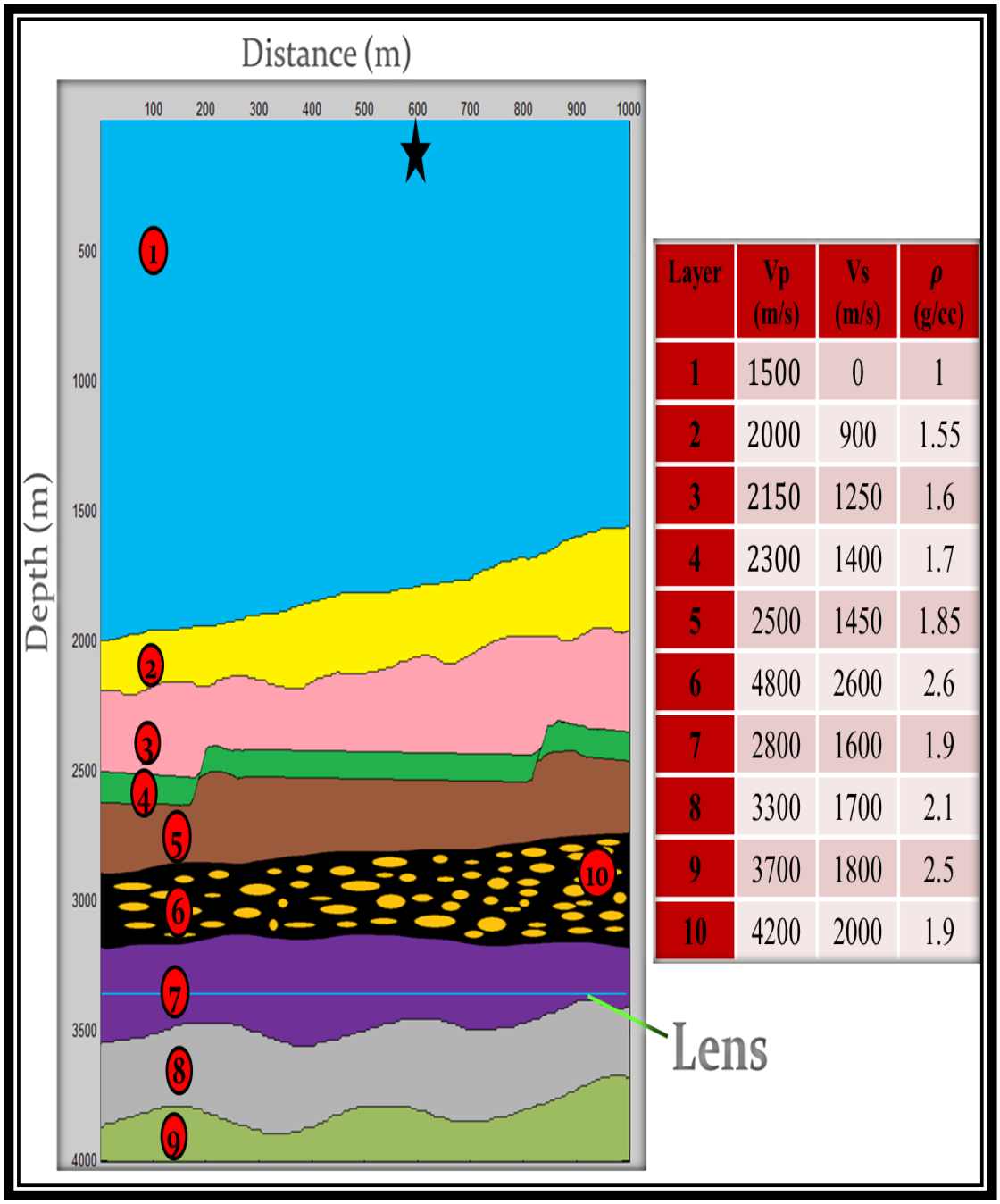

Layer	Vp (m/s)	Vs (m/s)	ρ (g/cc)
1	1500	0	1
2	2000	900	1.55
3	2150	1250	1.6
4	2300	1400	1.7
5	2500	1450	1.85
6	4800	2600	2.6
7	2800	1600	1.9
8	3300	1700	2.1
9	3700	1800	2.5
10	4200	2000	1.9

Figure 4.6. Geological construct of Northwest Australian basin-like model with lens in the sub-basalt layer, the elastic parameters for each layer is given to the right.

The corresponding un-interpreted borehole seismic data is shown in Figure 4.7. Similar to the borehole seismic data for model I, the lens is placed below the basalt layer. The receivers are placed from the 200 m mark to the 800 m mark. In other words the borehole seismic data spans 600 m in the x-axis. The duration of recording was 2.4 seconds.

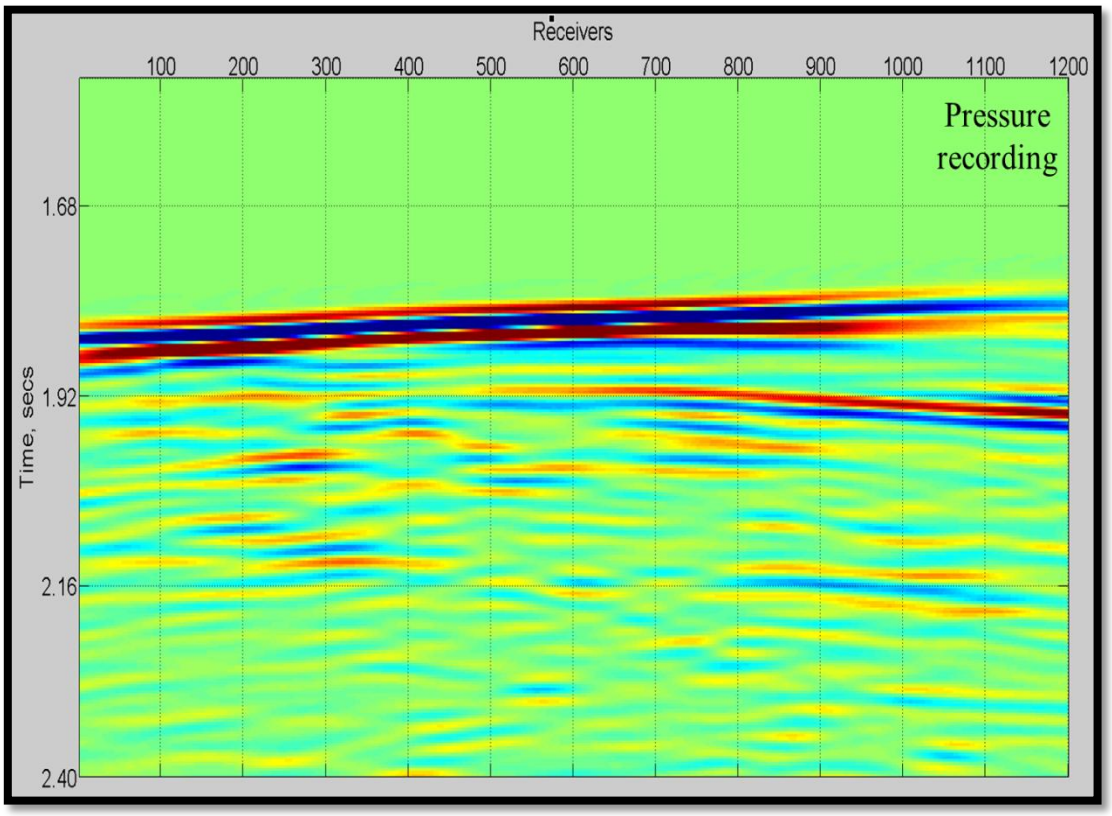

Figure 4.7. Borehole seismic data of Model II without interpretation.

Immediately obvious, looking at Figure 4.7 is the lack of continuity of events. There is no event, except for the direct arrival event (P_1) that can be interpreted throughout the data. The interpreted borehole seismic data is shown in Figure 4.8. This figure illustrates that we obtain almost the same travel times for the top of

layer 8 and layer 9 for model II as in model I. The similarity in the travel times is because the geology for both models (I and II) are the same except for the different basalt layers. We were unable to image across the entire section of the borehole seismic data.

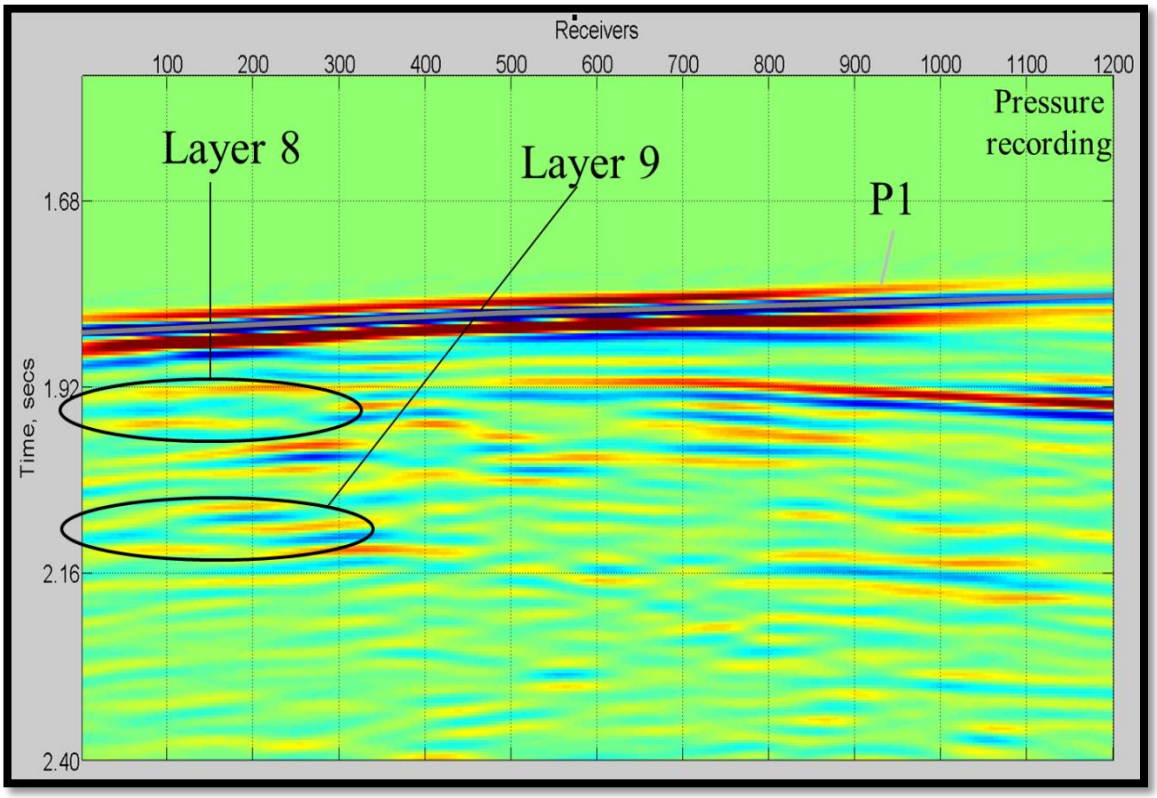

Figure 4.8. Interpreted borehole-like seismic data for horizontal receivers positioned in the sub-basalt layer for the Australian basin-like model.

We now consider the effect on the borehole seismic data for a lens with wash-outs placed at the 200th, 600th, and 1000th receiver positions, as shown in Figure 4.9. Again, similar to the borehole seismic data with wash-outs in model I, there are no visible, characteristic upside down 'V' shape events at the wash-out zones i.e. there are no tube waves seen on the data. The lack of any visible tube

waves were attributed to the limited energy that propagated in the sub-basalt layers and the relatively large wavelength, 196 times bigger than the wash-out zone, in the sub-basalt layer. The interpreted borehole seismic data with washout zones are shown in Figure 4.10.

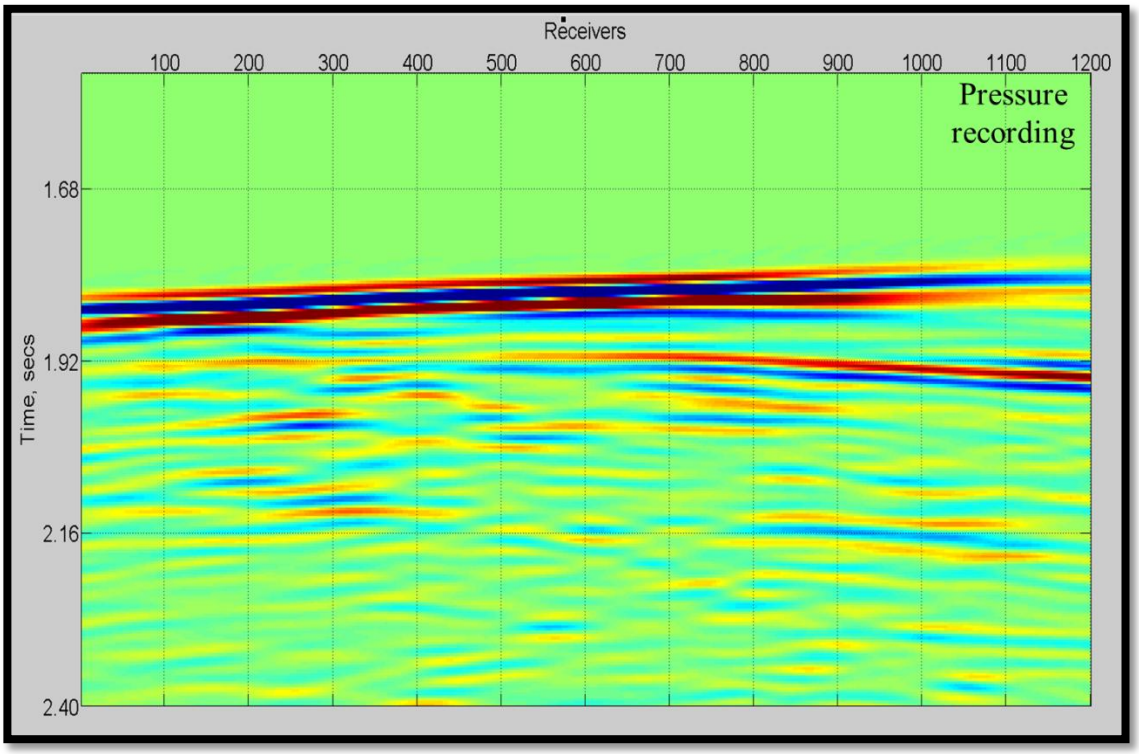

Figure 4.9. Borehole seismic data of Model II (washout zones) without interpretation.

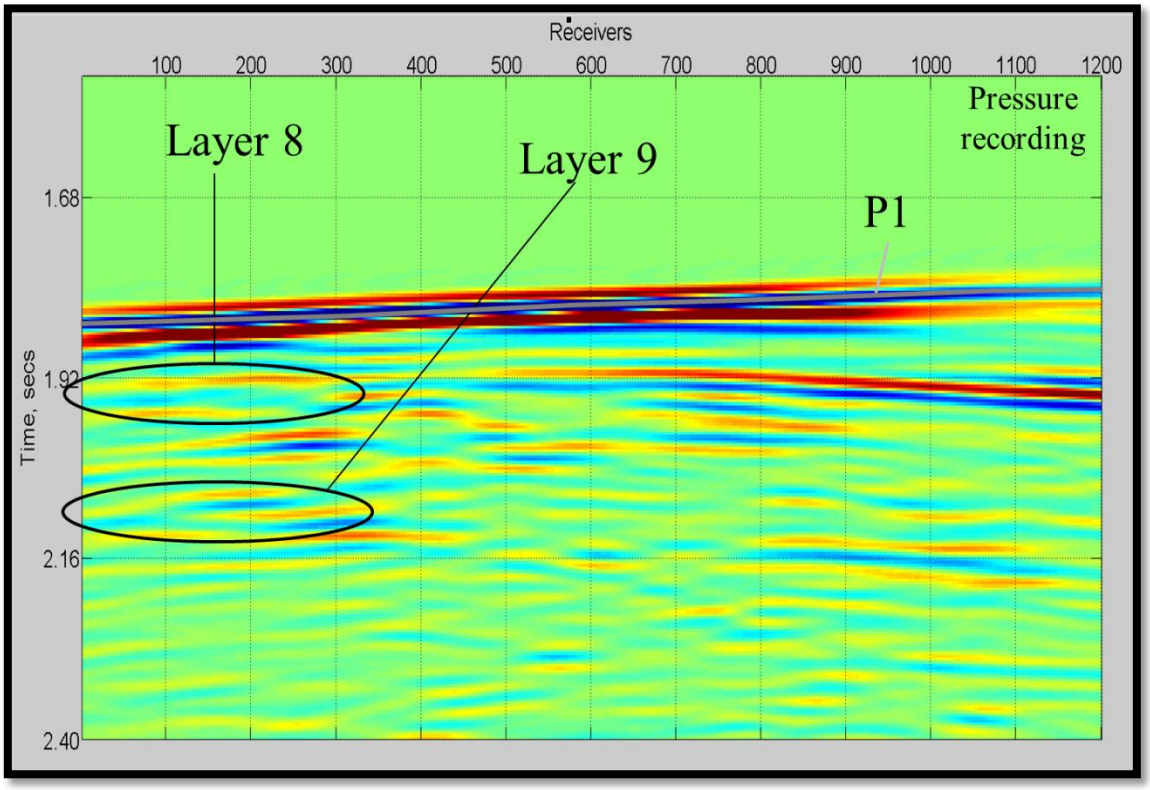

Figure 4.10. Borehole seismic data of Model II (washout zones) with interpretation.

An attempt was made to interpret any multiples with the sub-basalt layer. However, the data were so obscured that it was unsuccessful. The high amplitude event at two seconds was the effect of the boundary reflecting the source in the water layer. This event was labeled as the 'effect of the boundary' in Figure 4.5. It was interpreted by looking at the snapshots at various time intervals.

CHAPTER V

CONCLUSION

Below the sub-basalt layers, there is very little energy propagating, and the reflections and refractions are weak compared to the reflections above the basalt layer. The heterogeneous nature of the basalt layer and its irregular top and bottom surfaces scatter seismic energy, significantly contributing to the weak non-continuous reflectors.

On our borehole seismic data, we were not able to identify any of the sub-basalt layers throughout the section. Hence we concluded that borehole seismic data does not improve imaging below the basalt layers in ultra-deep waters. However, these results cannot be extended from the lens to the cylindrical borehole case because I used only one source. As discussed in Appendix B, we should have used many sources in the water column and then analyzed the data on a zero offset section.

No tube waves were seen on the borehole seismic data below the basalt layer from the wash-out zones. The lack of visible tube waves were attributed to the limited energy that propagated in the sub-basalt layers and the relatively large wavelength, 196 times bigger than the wash-out zone, in the sub-basalt layer. This result can be extended to the cylindrical borehole case. Our reasoning for this is; what enters the lens will enter the cylindrical borehole. How these tube waves behave may be different in either the lens or the cylinder, but what we can say for certain is that; if a tube waves enter the lens, the tube waves will enter the borehole. Therefore we conclude that in ultra-deep waters, below the basalt layer we will not expect to see any tube waves in the borehole.

The latter conclusion is important to the processing stage of borehole seismic data. Tube waves can mask possible reflections from sub-basalt layers. However, since they may not be visible in ultra-deep waters below basalt layers

then we will not have the problem of removing them in the processing stage; which can be quite difficult.

In addition, tube waves' best satisfy the cylindrical coordinate's wave equation, and therefore tube waves will be the best model using a finite-difference algorithm in cylindrical coordinates. However, we were limited by our computational resources and could not have done this. The thesis has nevertheless identified some of the complexities in ultra-deep waters and the problems associated with imaging below the basalt layer. It should provide a good foundation for more-advanced computation-intensive studies on borehole wave propagation.

REFERENCES

Geo Expro, 2007, Offshore Mid-Norway, I used this website to observe the seismic data offshore Mid-Norway basin, http://www.geoexpro.com/sfiles/5/13/5/file/seismic_II.pdf, June 2011.

Ikelle, T. L., and L. Amundsen, 2005, Introduction to petroleum seismology: Society of Exploration Geophysicists, Tulsa, Oklahoma, USA.

Levander, A. R., 1988, Fourth-order finite-difference P-SV seismograms: Geophysics, **53**, no. 11, 1425-1436.

Martini, F., R. W. Hobbs, C. J. Bean, and R. Single, 2005, A complex 3D volume of sub-basalt imaging: European Association of Geoscientists & Engineers, **23**, 41-51.

Moczo, P., J. Kristek, and L. Halada, 2004, The finite difference method for seismiologist: An introduction, Comenius University, Bratislava.

Oladeinde, O. A., 2005, Linear demultiple solution based on bottom multiple generator (BMG) reflector approximation: subsalt example: Geology/Geophysics department, College Station, Texas A&M University, Master of Science in Geophysics.

Singh, S. K., 2005, Sub-Basalt imaging: Modeling and demuliple: Geology/Geophysics department, College Station, Texas A&M University, Master of Science in Geophysics.

White, R. S., and D. McKenzie, 1989, The generation of volcanic continental margins and flood basalts: Journal of Geophysical Research, **94**, 7685–7729.

Supplemental Sources Consulted

Balch, A. M., and M. W. Lee, 1984, Vertical Seismic Profiling: Technique, Applications, and Case Histories: Boston (International Human Resources Development Corporation), 185-256.

Cheng, C., M. N. Toksov, and M. E. Willis, 1982c, Generation, propagation and analysis of tube waves in a borehole, Paper P: Trans. SPWLA 23rd Annual Logging Symposium, **1**.

Fliedner, M., and R. White, 2001, Seismic structure of basalt flows from surface seismic data, borehole measurements, and synthetic seismogram modeling: Geophysics, **66**, no. 6, 1925-1936.

Gal'perin, E. I., 1974, Vertical Seismic Profiling: Society of Exploration Geophysicists Special Publication, No. 12, Tulsa, 270 pages.

Hardage, B. A., 2000, Vertical Seismic Profiling: Priniciples: Third updated and revised edition, Handbook of Geophysical Exploration, **14**, 104-128.

Madariaga, R., 1976, Dynamics of an expanding circular fault, Bulletin of the Seismological Society of America, **66** no. 3: 639 -666.

Planke, S., and G. U. Haugen, 2001, Seismic imaging and interpretation of volcanic constructions: Volcanic Basin Petroluem Research, Statoil, Oslo, Norway.

Toksov, M. N., and C. Cheng, 1981a, Elastic wave propagation in a fliud-filled borehole and synthetic acoustic logs: Geophysics, **46**, 1042-1053

Toksoz, M., and R. Stewart, 1984, Vertical Seismic Profiling, Part B: Advanced Concepts: Geophysical Press, **14B**, 256-299.

White, J.E., 1965, Seismic waves- radiation, transmission, and attenuation: McGraw-Hill, New York, 302 pages.

APPENDIX A

Introduction

The interior of the Earth is considerably complex and consist of laterally heterogeneous layers of different materials. Analytical methods do not provide solutions of the equation of motion for sufficiently realistic models of the Earth. Therefore approximate numerical methods have to be used.

There are several full wave methods that numerically model seismic responses of the Earth. The solution of these full-wave methods involves discretization of the wave equation. In other words, these methods do not approximate the solution but rather approximate the equation.

The Wave equation is: $\frac{\partial}{\partial x_j}\left(C_{ijkl}\frac{\partial u_l}{\partial x_k}\right) = \rho\frac{\partial^2 u_i}{\partial t^2}$ *for i, j= 1, 2, 3..*(A1)

where: C_{ijkl} is the elasticity tensor

U_i is the i^{th} component of displacement

t is time

x_j is the j^{th} Cartesian coordinates

Full-wave methods find ways to solve the wave equation directly on computers either from:

1. Transforming continuous partial derivatives into an algebraic equation or
2. Transforming the model (computational domain) into geometric objects.

In this thesis we will be using Finite difference method to numerically model seismic responses of the Earth. It is one of the most successful techniques to

simulate elastic wave propagation through complex media once the differential approximations used are correct. It can accurately predict travel times and amplitudes of primaries, multiples, diffractions and converted waves, and hence closely simulate the real earth's response.

Finite Difference Method

The finite difference technique is by far the most accurate tool for simulating elastic wave propagation when an adequate discretization in space and time is possible, that gives an accurate computation of derivatives of the wave equation (Ikelle and Amundsen 2005).

The application of the method involves (Moczo et al. 2004):

1. The construction of a discrete finite difference model:
    i. Construction of a system of the finite difference equation, which covers the computational domain of space and time,
    ii. Approximations to derivatives, initial conditions and boundary conditions all at the grid points
2. Analysis of the finite difference model
    i. Stability of the finite difference modeling,
    ii. Grid dispersion in finite difference modeling
3. Numerical Computations

To elaborate on the finite difference method we start by recalling the building equations of this method, "The equations for elastodynamic wave motion".

Equations for Wave Propagation in Elastic Media

The equations used in the finite difference method to model wave propagation are:

1. The equations of conservation of momentum: (for simplicity the 2D formulation is shown).
    a. $\rho(\boldsymbol{x})\partial_t v_x(\boldsymbol{x},t) - \{\partial_x \tau_{xx}(\boldsymbol{x},t) + \partial_z \tau_{xz}(\boldsymbol{x},t)\} = f_x(\boldsymbol{x},t)$ … (A2)
    b. $\rho(\boldsymbol{x})\partial_t v_z(\boldsymbol{x},t) - \{\partial_x \tau_{xz}(\boldsymbol{x},t) + \partial_z \tau_{zz}(\boldsymbol{x},t)\} = f_z(\boldsymbol{x},t)$ … (A3)

where:

v= $\{v_x(x,t), v_z(x,t)\}$ are the particle velocity, i.e $\partial_t u_x(\boldsymbol{x},t) = v_x(\boldsymbol{x},t)$ and $\partial_t u_z(\boldsymbol{x},t) = v_z(\boldsymbol{x},t)$,

$\rho(\boldsymbol{x})$ is the material density,

$\boldsymbol{\tau} = \{\tau_{xz}(x,t), \tau_{xx}(x,t), \tau_{zz}(x,t)\}$ are the stress components,

$\boldsymbol{f} = \{f_x(x,t), f_z(x,t)\}$ are the components of the body forces.

2. For a linearly elastic isotropic medium the stress-strain relationship is:
    a. $\partial_t \tau_{xx}(\boldsymbol{x},t) = [\lambda(\boldsymbol{x}) + 2\mu(\boldsymbol{x})]\partial_x v_x(\boldsymbol{x},t) + \lambda(\boldsymbol{x})\partial_z v_z(\boldsymbol{x},t) + I_{xx}(\boldsymbol{x},t)$ … (A4)
    b. $\partial_t \tau_{zz}(\boldsymbol{x},t) = [\lambda(\boldsymbol{x}) + 2\mu(\boldsymbol{x})]\partial_z v_z(\boldsymbol{x},t) + \lambda(\boldsymbol{x})\partial_x v_x(\boldsymbol{x},t) + I_{zz}(\boldsymbol{x},t)$ … (A5)
    c. $\partial_t \tau_{xz}(\boldsymbol{x},t) = \mu(\boldsymbol{x})[\partial_z v_x(\boldsymbol{x},t) + \partial_x v_z(\boldsymbol{x},t)] + I_{xz}(\boldsymbol{x},t)$ … (A6)

where:

$\lambda(\boldsymbol{x})$: No simple physical explanation
$\mu(\boldsymbol{x})$: Shear modulus
} Lame' Parameters

$I = \{I_{xx}(\boldsymbol{x}, t), I_{zz}(\boldsymbol{x}, t), I_{xz}(\boldsymbol{x}, t)\}$ are the stress forces which act at the surface of the medium. These forces are associated with volumetric and/or angular deformation.

3. Equations (A2),(A3),(A4),(A5),(A6), are the first order elastodynamic equations of motion. To solve these equations we must specify both the initial and the boundary conditions.
    a. The initial conditions exhibit the causality rule, where all fields are null before the source is fired, i.e. the stress, particle velocity and their time derivatives are equal to zero at 't ≤ 0'.
        i. $v = \partial_t v = 0,$ $t \leq 0$ … (A7)
        ii. $\tau = \partial_t \tau = 0,$ $t \leq 0$ … (A8)
    b. The boundary conditions can be either absorbing boundary or free-surface condition at z=0, while the rest of the medium is unbounded. For the case of an air-water free-surface planar boundary at z=0:
        i. $\tau_{zz}(x, z = 0, t) = \tau_{xz}(x, z = 0, t) = 0$ … (A9)

Discretization in Time and Space

Discretization, in mathematics, concerns the process of converting continuous models and equations into discrete counterparts. This process is an essential step towards making successful numerical models. The finite difference algorithm discretizes both time and space as follows:

$$\begin{aligned} t &= n\Delta t, & n &= 0, 1, 2, \dots, N, \\ x &= i\Delta x, & i &= 0, 1, 2, \dots, N, \\ z &= i\Delta x, & k &= 0, 1, 2, \dots, N \end{aligned} \qquad \dots(A10)$$

This is known as discretization of the reference grid. Each quantity in the finite difference equations (A2), (A3), (A4), (A5), (A6), can be defined by functions of the indexes n, i, and k. The finite difference method used in this thesis utilizes the staggered-grid technique. This implementation does not grid all quantities on the reference grid, some quantities are defined on half grid points off the reference grid. The quantities defined by the staggered grid techniques are depicted in Figure A.1.

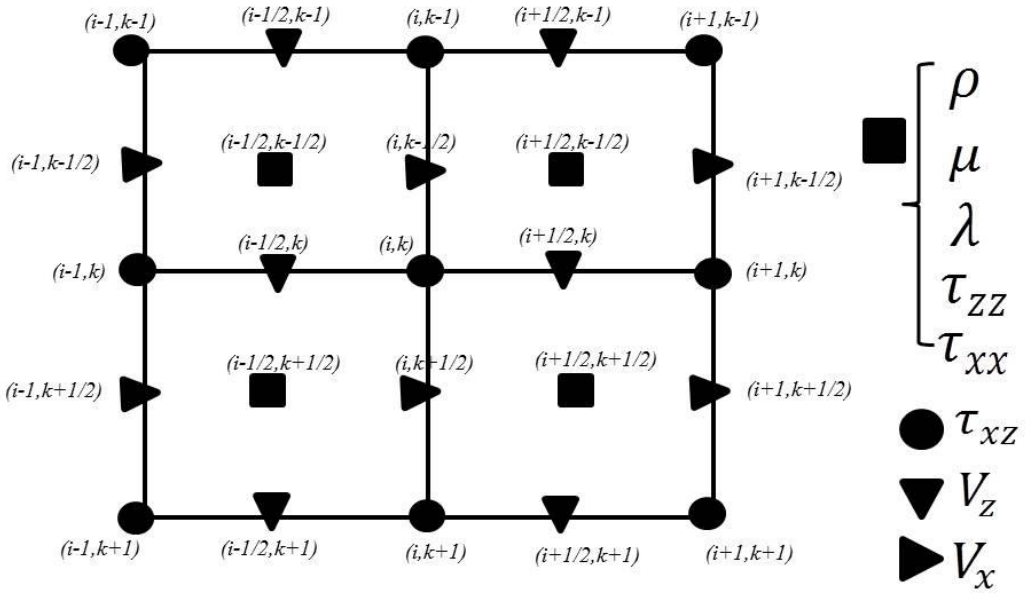

Figure A.1: Showing the staggered grid for 2D finite difference modeling.

The definition of each quantity on the staggered grid is as follows, starting with the material properties:

$$(x,z) = \lambda\left[\left(i+\tfrac{1}{2}\right)\Delta x, \left(k+\tfrac{1}{2}\right)\Delta x\right] = \lambda_{1+1/2,k+1/2} \quad \text{... (A11)}$$

$$\mu(x,z) = \mu\left[\left(i+\tfrac{1}{2}\right)\Delta x, \left(k+\tfrac{1}{2}\right)\Delta x\right] = \mu_{1+1/2,k+1/2} \quad \text{... (A12)}$$

$$\rho(x,z) = \rho\left[\left(i+\tfrac{1}{2}\right)\Delta x, \left(k+\tfrac{1}{2}\right)\Delta x\right] = \rho_{1+1/2,k+1/2} \quad \text{... (A13)}$$

Particle Velocity:

$$v_z(x,z,t) = v_z[(i+\tfrac{1}{2})\Delta x, (k)\Delta x], = [v_z]^{n+1/2}_{i+1/2,k} \quad \text{... (A14)}$$

$$v_x(x,z,t) = v_x\left[(i)\Delta x, \left(k+\tfrac{1}{2}\right)\Delta x\right] = [v_z]^{n+1/2}_{i,k+1/2} \quad \text{... (A15)}$$

Stresses:

$$\tau_{zz}(x,z,t) = \tau_{zz}\left[\left(i+\tfrac{1}{2}\right)\Delta x, \left(k+\tfrac{1}{2}\right)\Delta x\right] = [\tau_{zz}]^{n}_{i+\frac{1}{2},k+\frac{1}{2}} \quad \text{... (A16)}$$

$$\tau_{xz}(x,z,t) = \tau_{xz}[(i)\Delta x, (k)\Delta x], = [\tau_{xz}]^{n}_{i,k} \quad \text{... (A17)}$$

In the staggered grid implementation the temporal and time derivatives are calculated differently. The time derivative uses a three point formula, which is a second order difference operator. The time derivative is as follows, adapted from Abramowitz and Stegun (1964):

$$\partial_x g(x) \approx \frac{1}{\Delta x}\left[\frac{1}{2}g(x+\Delta x) - \frac{1}{2}g(x-\Delta x)\right] \quad \text{... (A18)}$$

On the other hand, the spatial derivatives are calculated using the five point formula, which is a fourth order difference operator. The spatial derivative adapted from Abramowitz and Stegun (1964) is written as:

$$\partial_x g\left(x+\tfrac{1}{2}\Delta x\right) = \frac{1}{\Delta x}\left[\frac{1}{24}\big(g(x+2\Delta x) - g(x-2\Delta x)\big) + \frac{9}{8}\big(g(x+\Delta x) - g(x-\Delta x)\big)\right] \quad \text{... (A19)}$$

These difference operators in the staggered grid implementation transform the set of equations (2) through (6) to:

Equation (2) transformation will be elaborated on while the other transformations will be stated.

Firstly, identify temporal derivatives: $[\partial_t v_z]\,]^n_{i,k+1/2} = \Delta t\{[v_x]^{n+1/2}_{i,k+1/2} - [v_x]^{n-1/2}_{i,k+1/2}\}$ … (A20)

Notice the temporal derivatives as well as the superscript quantities.

The spatial derivatives will be better understood by an illustration to explain the fourth order difference operator:

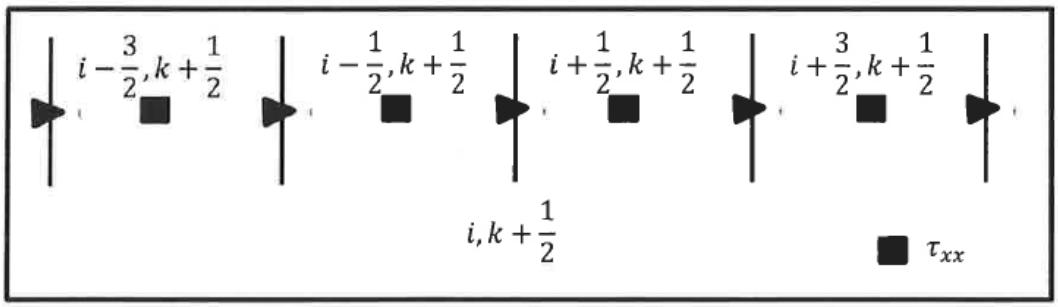

Figure A.2: Shows an illustration of the staggered grid technique to determine the spatial derivatives.

Figure A.2 shows that the vertical particle velocity is centered about the normal horizontal stress component at different spatial positions. Also, from the figure the normal horizontal stress component is written as:

$$[\partial_x \tau_{xx}\ ]^n_{i,k+1/2} = b\ (\frac{1}{24}\{[\tau_{xx}]^n_{i+3/2,k+1/2} - [\tau_{xx}]^n_{i-3/2,k+1/2}\} + \frac{9}{8}\Big\{[\tau_{xx}]^n_{i+1/2,k+1/2} - [\tau_{xx}]^n_{i-1/2,k+1/2}\Big\} \quad \text{... (A21)}$$

$$\text{where } b = {}^{1}\Big/\Delta x \rho_{i,k+1/2} \quad \text{... (A22)}$$

The following are some of the basic output equations in the finite difference staggered grid algorithm:

Vertical Particle Velocity: $[v_z]^{n+1/2}_{i+1/2,k} = [v_z]^{n-1/2}_{i+1/2,k} + \alpha_{i+1/2,k}$

$$\Big[\Big(\frac{1}{24}\Big\{[\tau_{zz}]^n_{i+1/2,k+3/2} - [\tau_{zz}]^n_{i+1/2,k-3/2}\Big\} + \frac{9}{8}\Big\{[\tau_{zz}]^n_{i+1,k} - [\tau_{zz}]^n_{i,k}\Big\}\Big) + \Big(\frac{1}{24}\{[\tau_{xz}]^n_{i+2,k} - [\tau_{xz}]^n_{i-1,k}\} + \frac{9}{8}\{[\tau_{xz}]^n_{i,k+1/2} - [\tau_{xz}]^n_{i,k-1/2}\}\Big) + [f_z]^n_{i+1/2,k}\Big] \quad \text{... (A23)}$$

Horizontal Particle Velocity: $[v_z]^{n+1/2}_{i+1/2,k} = [v_z]^{n-1/2}_{i+1/2,k} + \alpha_{i,k+1/2}$

$$\Big[\Big(\frac{1}{24}\Big\{[\tau_{zz}]^n_{i+1/2,k+3/2} - [\tau_{zz}]^n_{i+1/2,k-3/2}\Big\} + \frac{9}{8}\Big\{[\tau_{zz}]^n_{i+1,k} - [\tau_{zz}]^n_{i,k}\Big\}\Big) + \Big(\Big\{\frac{1}{24}[\tau_{xz}]^n_{i+2,k} - [\tau_{xz}]^n_{i-1,k}\Big\} + \Big\{\frac{9}{8}[\tau_{xz}]^n_{i,k+1/2} - [\tau_{xz}]^n_{i,k-1/2}\Big\}\Big) + [f_z]^n_{i+1/2,k}\Big] \quad \text{... (A24)}$$

Where: $\alpha_\gamma = \frac{\Delta t}{\Delta x \rho_\gamma}$

Horizontal Normal Stress(x-direction): $[\tau_{xx}]^{n+1}_{i+1/2,k+1/2} = [\tau_{xx}]^n_{i+1/2,k+1/2} + \frac{\Delta t}{\Delta x}$

$$\Big[\Big[\Big[\ (\lambda + 2\mu)_{i+1/2,k+1/2}\Big\{\frac{1}{24}\Big([v_x]^{n+1/2}_{i+1/2,k+2} - [v_x]^{n+1/2}_{i+1/2,k-1}\Big) + \frac{9}{8}\Big([v_x]^{n+1/2}_{i+1/2,k+1} - [v_x]^{n+1/2}_{i+1/2,k}\Big)\Big\}\Big] + \Big[\lambda_{i+1/2,k+1/2}\Big\{\frac{1}{24}\Big([v_z]^{n+1/2}_{i+2,k+1/2} - [v_z]^{n+1/2}_{i-1,k+1/2}\Big) + \frac{9}{8}\Big([v_z]^{n+1/2}_{i+1,k+1/2} - [v_z]^{n+1/2}_{i,k+1/2}\Big)\Big\}\Big] + I_{xx}(\boldsymbol{x}, t)\ \Big] \quad \text{... (A25)}$$

Vertical Normal Stress (z-direction): $[\tau_{zz}]^{n+1}_{i+1/2,k+1/2} = [\tau_{zz}]^n_{i+1/2,k+1/2} + \frac{\Delta t}{\Delta x}$

$$\left[\left[\left[(\lambda + 2\mu)_{i+1/2,k+1/2} \left\{\frac{1}{24}\left([v_z]^{n+1/2}_{i+1/2,k+2} - [v_z]^{n+1/2}_{i+1/2,k-1}\right) + \frac{9}{8}\left([v_z]^{n+1/2}_{i+1/2,k+1} - [v_z]^{n+1/2}_{i+1/2,k}\right)\right\}\right] + \left[\lambda_{i+1/2,k+1/2} \left\{\frac{1}{24}\left([v_x]^{n+1/2}_{i+2,k+1/2} - [v_x]^{n+1/2}_{i-1,k+1/2}\right) + \frac{9}{8}\left([v_x]^{n+1/2}_{i+1,k+1/2} - [v_x]^{n+1/2}_{i,k+1/2}\right)\right\}\right] + I_{zz}(\boldsymbol{x}, t)\right] \quad \text{... (A26)}$$

Shear Stress:

$$[\tau_{xz}]^{n+1}_{i,k} = [\tau_{xz}]^{n}_{i,k} + \frac{\Delta t}{\Delta x}\{(\mu)_{i,k}\}\left[\left[\frac{1}{24}\left([v_x]^{n+1/2}_{i,k+3/2} - [v_x]^{n+1/2}_{i,k-3/2} + [v_z]^{n+1/2}_{i+3/2,k} - [v_z]^{n+1/2}_{i-3/2,k}\right)\right] + \left[\frac{9}{8}\left([v_x]^{n+1/2}_{i,k+1/2} - [v_x]^{n+1/2}_{i,k-1/2} + [v_z]^{n+1/2}_{i+1/2,k} - [v_z]^{n+1/2}_{i-1/2,k}\right)\right] + I_{xz}(\boldsymbol{x}, t)\right] \quad \text{... (A27)}$$

Staggered Grid Benefits

The staggered grid naturally centers its operators in both time and space as seen from Figure A.2 and A.3. Equation A21 through A27 shows that, the differential operators do not act on the medium operators but only on the wave-field parameters of velocity and stress. Consequently the medium geologic complexity will have no bearing on the differential terms. In addition, this scheme staggers both temporally and spatial, hence the particle velocity is updated independently from stresses, in one step, making the procedure more efficient. Also, from the ICASP vol. 8, 2002, the associated benefits of this procedure are:

i. Stability for all values of Poisson ratio,
ii. Minimized grid dispersion and grid anisotropy,
iii. Ability to simulate surface or buried sources,
iv. Ability to simulate free surface boundary conditions.

Stability and Dispersive Conditions in Finite Difference Modeling

In numerical modeling, iterative procedures time step by time step introduce instabilities in the data. The instability conditions are given by:

$$\Delta t < 0.606 \frac{\Delta x}{V_{max}};$$ (Levander, 1988)

The dispersion condition is errors due to the spatial derivatives, given by:

$$\Delta x < \frac{V_{min}}{5 f_{max}};$$ (Levander, 1988)

The Capabilities of the FDM

The FDM method has much functionality. Over the course of this thesis some of the capabilities of the FDM that have been learnt are:

- Control on Acquisition geometry
- Control on source mechanism
- Physical quantity being measured
- Control on modeling the geology
- Can create seismic sections and wave propagation snapshots
- Can mathematical produce and measure theoretical quantities

APPENDIX B

Exploring Ultra-deep Waters

In ultra-deep waters, reservoirs are can be located below salts or below basalt layers. However the present imaging technology of towed streamer data or ocean bottom survey data does not yet tell us where to drill in these regions. In this section we will discuss the challenges associated with imaging either below salt or below basalt. We will first begin with exploring subsalt.

Exploring Subsalt

It is well established that potential reservoirs in salt provinces are located either below the salt domes or on the flanks of the salt domes. The main reasons for the location of these reservoirs are that: salt is by nature a very good top seal of these reservoirs and salt diapirism can create structural and stratigraphic traps on the diapirs flanks. In this section we will consider an example of synthetic data illustrating the difficulty of imaging below salt. The 2D geologic model is shown in Figure B.1. The salt model is similar to the geology we will expect to find in the Gulf of Guinea. The geologic model was inputted in a finite difference program to simulate synthetic towed streamer acquisition. As expected the shots were placed along the free surface together with the receivers. There were 320 shots at a shot interval of 12.5 m. The data was obtained from Oladeinde, 2005.

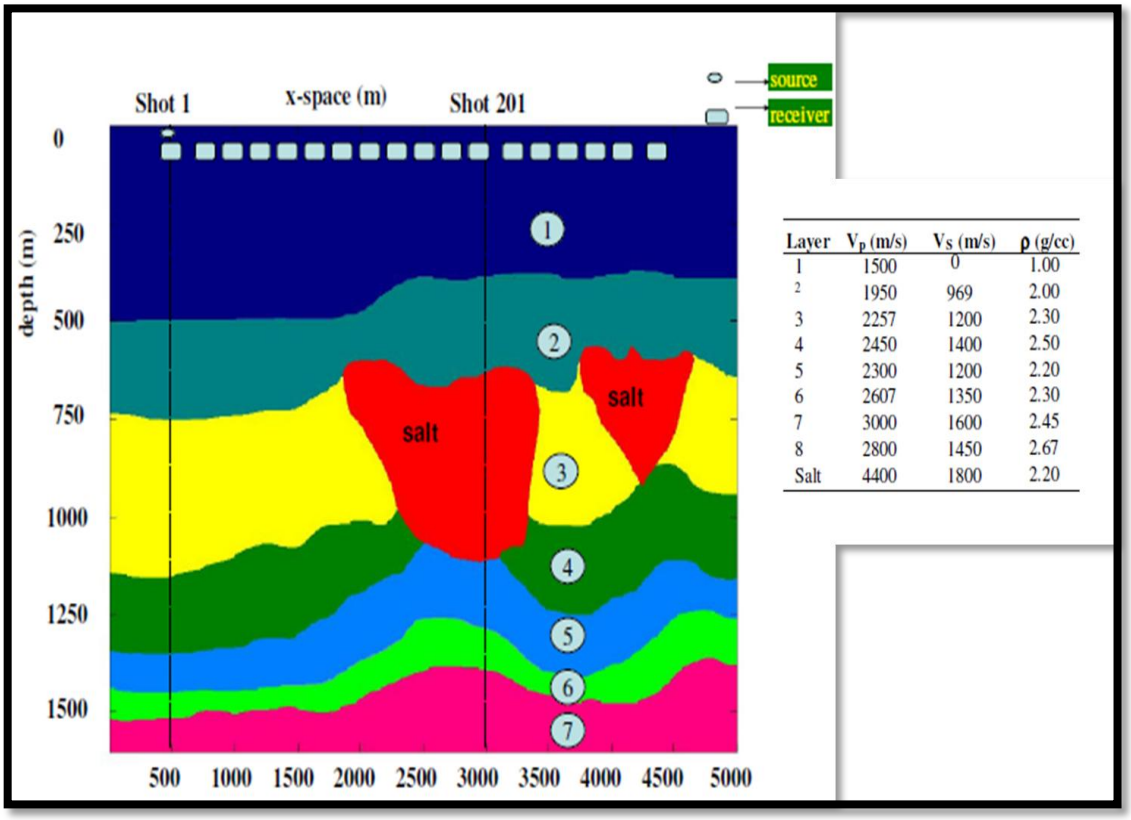

Layer	V_P (m/s)	V_S (m/s)	ρ (g/cc)
1	1500	0	1.00
2	1950	969	2.00
3	2257	1200	2.30
4	2450	1400	2.50
5	2300	1200	2.20
6	2607	1350	2.30
7	3000	1600	2.45
8	2800	1450	2.67
Salt	4400	1800	2.20

Figure B.1. Geologic model of salt complexes for a towed streamer acquisition, Oladeinde, 2005.

The corresponding towed streamer seismic data is illustrated in Figure B.2. The seismic data is a zero offset section. The layers above the salt or far away from the salt had clear associated events as labeled in Figure B.2. Interpreting below the salt or close to the flanks of the salt is very difficult. No clear events from the subsalt layers were able to be interpreted below the salt domes. There were some events; however these events were associated with free surface multiples in the data. The free surface multiples can mask the subsalt events, therefore Oladeinde, 2005, removed the multiples from the data as shown in Figure B.3. However, the removal of the multiples did not make imaging below the salt domes easier.

The poor imaging below the salt can be attributed to the limited seismic energy propagating into the subsalt layers. This is because; the irregular shape of the salt lenses can disperse seismic energy reducing down-going seismic energy and the high velocity of the salt reflects most of the incoming seismic energy upwards. In other words, there will be weak reflections from the subsalt layers.

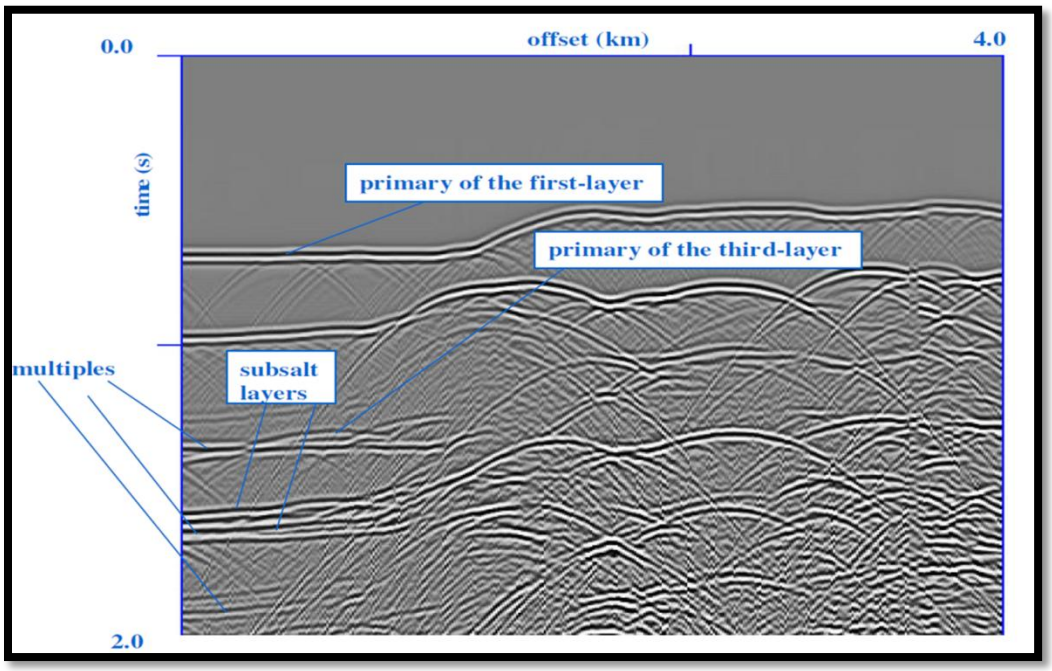

Figure B.2. Towed streamer seismic data illustrating the poor imaging below the salt domes, this data is a zero offset section, Oladeinde, 2005.

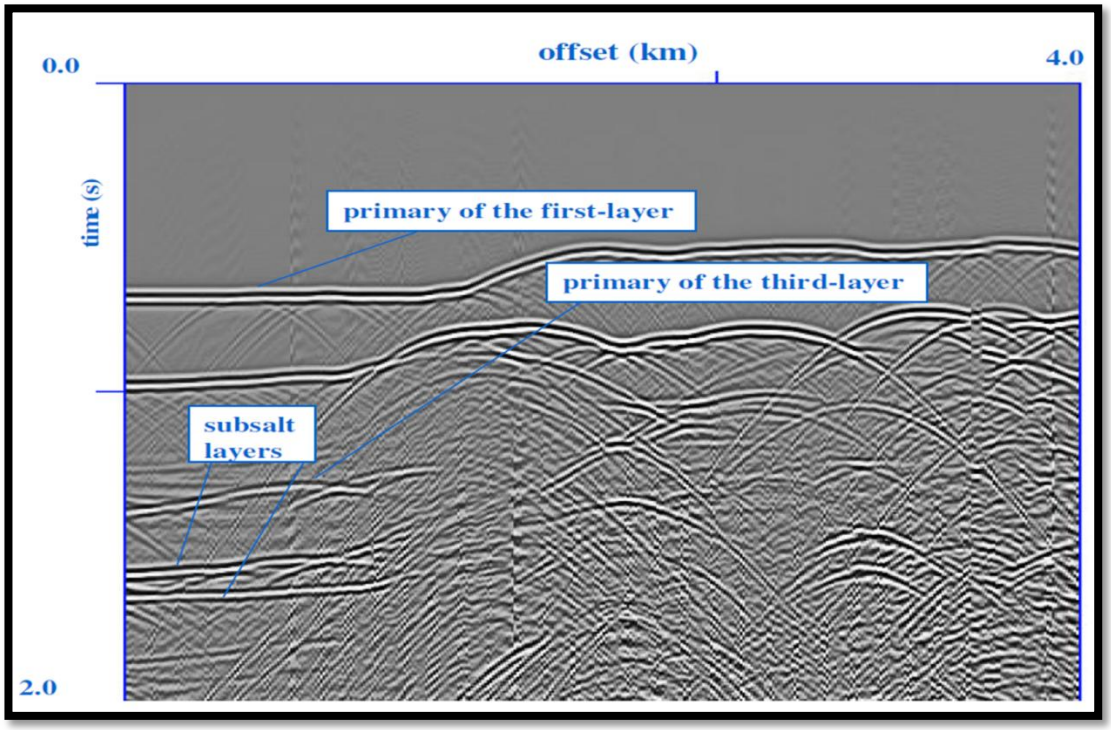

Figure B.3. Demultipled towed streamer seismic data illustrating the poor imaging below the salt domes; this data is a zero offset section, Oladeinde, 2005.

We will now briefly discuss what multiples are before we proceed to look at imaging below basalt layers. In marine acquisition, two types of multiples occur, internal multiples and free surface multiples. Internal multiples are defined as having at least one bounce for a seismic wave, between two layers in the subsurface, as shown in Figure B.4. Internal multiples can occur in different orders. For instance, when there is one bounce between two subsurface layers, this is called a first order internal multiple. The orders of internal multiples are shown in Figure B.4.

A free surface multiple is defined as a seismic wave having at least one bounce from the free surface. Similar to internal multiples, free surface multiples also occur in different orders as shown in Figure B.5.

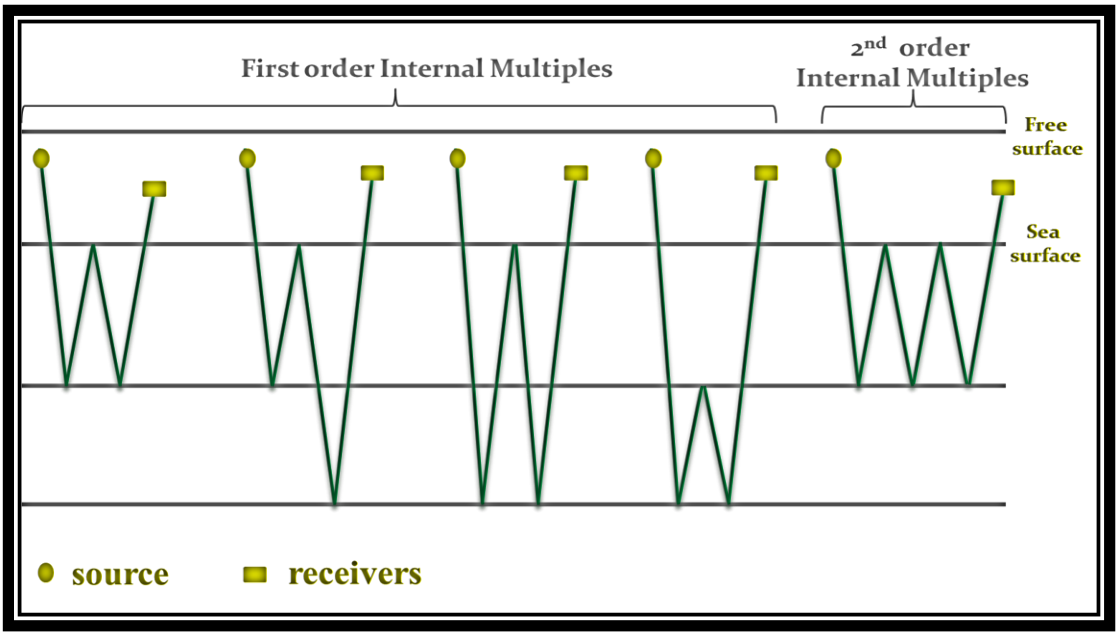

Figure B.4. Schematic of internal multiples.

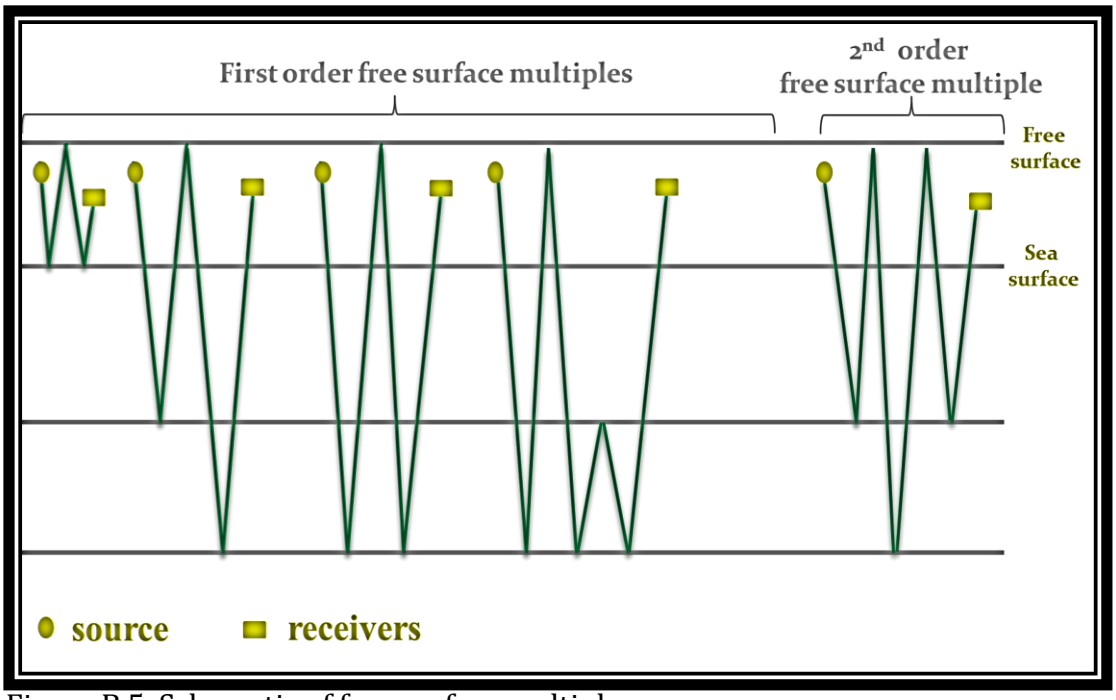

Figure B.5. Schematic of free surface multiples.

Exploring Sub-basalt

It is also well established that there are large reserves of oil and gas below basalt rocks. Generally these basins are located in ultra-deep waters. In this section we will show ocean bottom seismic data, Singh, 2005. Singh, 2005, used a 2D geologic model, as shown in Figure B.6. In this model, the basalt layer is inter-bedded with thin clay layers. As expected, the sources are placed close to the free surface while the receivers are placed on the sea-floor. Figure B.6, also shows the type of multiple events that are expected in ocean bottom acquisition.

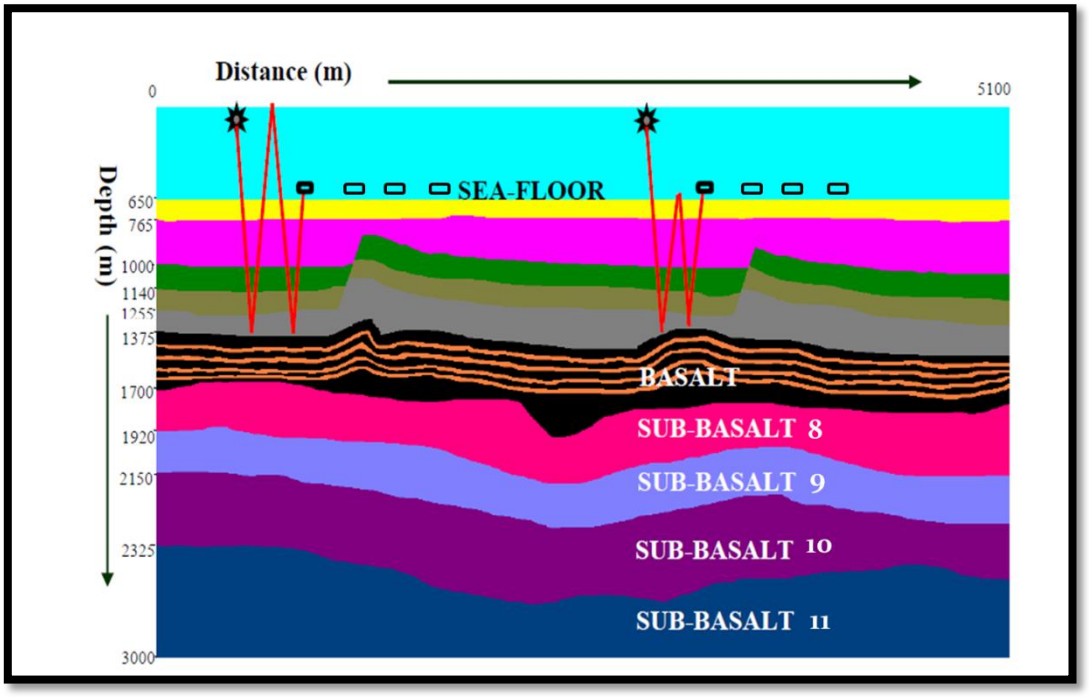

Figure B.6. Illustrating the geological construct of ocean bottom seismic acquisition, Singh, 2005.

The corresponding seismic data is shown in Figure B.7. This figure is a zero offset section of the ocean bottom seismic data.

Figure B.7. Zero offset ocean bottom seismic data.

The ocean bottom seismic picture in Figure B.7, is dominated by free surface multiples. The figure also has the interpretation of where the sub-basalt layers should be. It is clear that interpreting below the sub-basalt layers is difficult. Even when the free surface multiples are removed from the data, Figure B.8, we are still unable to clearly identify the sub-basalt layers. The reasons for the poor imaging are mainly due to the scattering of incoming seismic energy from the heterogeneous basalt layer and the highly reflective top surface of the basalt layer.

Now that we have present two examples of conventional seismic data, it is obvious that we are not able to imaging below the basalt and salt layers using current seismic imaging technology.

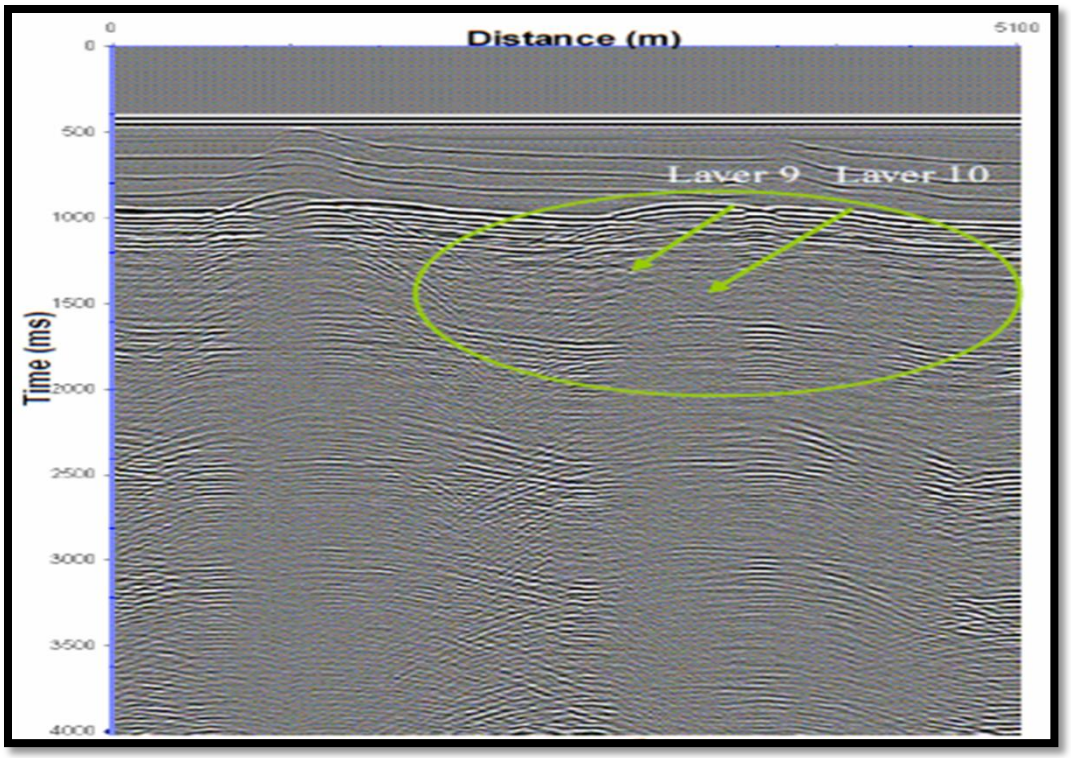

Figure B.8. Demultipled zero offset ocean bottom seismic data.

VITA

Name: Satyan Singh

Address: Texas A&M University, Halbouty, Rm 365, Department of Geology and Geophysics, MS 3115, College Station, Texas, 77843-3115.

Email Address: satyansinghster@gmail.com

Education: B.S. Petroleum Geosciences, University of the West Indies, St. Augustine, June 2005

M.S. Geophysics, Texas A&M University, December 2011